Chemical Science

ROYAL SOCIETY OF CHEMISTRY

EDGE ARTICLE

View Article Online
View Journal | View Issue

Cite this: *Chem. Sci.*, 2025, **16**, 5857

All publication charges for this article have been paid for by the Royal Society of Chemistry

Thermal- and light-induced valence tautomerism with a concerted spin transition in an iron tris(diimine) complex†

Jett T. Janetzki, [a] Dominic S. Brown, [a] Florian Daumann, [b] I. Haseena Ismail, [a] Robert W. Gable, [a] Moya A. Hay, [a] Roger J. Mulder, [c] Alyona A. Starikova, [d] Birgit Weber, [b] Marcus J. Giansiracusa [a] and Colette Boskovic *[a]

The switching phenomena of spin crossover (SCO) and valence tautomerism (VT) are respectively dominated by iron(II) and cobalt-dioxolene systems. To explore new possibilities for SCO or VT, the redox-active α-diimine ligand bis((phenyl)imino)acenaphthene (Ph-BIAN), which can adopt neutral (L^0), monoanionic ($L^{\bullet-}$), and dianionic (L^{2-}) states, was paired with zinc, cobalt, manganese and iron to give $[M(Ph\text{-}BIAN)_3](BPh_4)_2$ (M = Zn (**1**), Co (**2**), Mn (**3**), Fe (**4**)). Compounds **1**, **2** and **3** adopt a temperature invariant $M^{II}\text{-}(L^0)_3$ state, (**2** and **3** are high spin (HS)) in the solid- and solution-states. Electrochemical measurements show the metal controls the degree of electronic communication between the Ph-BIAN ligands. In stark contrast to **1**, **2** and **3**, compound **4** adopts the LS-$Fe^{III}\text{-}(L^{\bullet-})(L^0)_2$ (LS = low spin) tautomeric form as the ground state in both the solid-state and in solution. Combined variable temperature solid- and solution-state structural, Mössbauer and electronic spectroscopy, and magnetic measurements, show that **4** undergoes the thermally-induced VT process LS-$Fe^{III}\text{-}(L^{\bullet-})(L^0)_2 \rightleftharpoons$ HS-$Fe^{II}\text{-}(L^0)_3$, the only example of VT accompanied by a concerted spin transition in an iron complex with a redox-active ligand. Solid-state photomagnetic measurements suggest that the VT interconversion is also induced by light. Light-induced VT has not been previously observed for complexes other than cobalt-dioxolene, and is potentially afforded here by the unique spin-state change that results in large differences in the Fe–N bond lengths for the two valence tautomers. This study introduces a new example of VT, and suggests that optically-induced VT can be displayed by iron systems, opening alternate pathways toward molecular switches that can be controlled with multiple stimuli.

Received 17th November 2024
Accepted 22nd February 2025

DOI: 10.1039/d4sc07798a

rsc.li/chemical-science

Introduction

The capability of earth abundant 3d transition metals to access multiple oxidation- and spin-states has led to the synthesis of complexes that interconvert between distinct electronic states. These switchable molecules are key synthetic targets in efforts to miniaturize and improve current technologies, with applications in sensors, displays, actuators, and electronics and spintronics.[1–7] A classic example of molecular switching is spin crossover (SCO), in which a metal complex interconverts between the low spin (LS) and high spin (HS) states.[8] Incorporation of a redox-active ligand opens additional possibilities for modulating the electronic and magnetic properties of a metal complex. In certain circumstances, metal complexes with a redox-active ligand can undergo valence tautomerism (VT), in which a reversible intramolecular electron transfer occurs between the redox-active metal and redox-active ligand.[9,10] Valence tautomerism is akin to metal-to-metal electron transfer, commonly termed charge-transfer-induced spin transition (CTIST), which is observed in Prussian blue analogues.[11] In this study, VT refers solely to electron transfer between a metal and organic ligand. Both SCO and VT are induced by stimuli such as temperature, light, or pressure.[8,9,12–14]

Spin crossover is most commonly observed for octahedral Fe(II) compounds with an N_6 coordination sphere.[8] More recently, SCO in Fe(III) complexes, usually evident with a N_4O_2-coordination, has

[a]*School of Chemistry, University of Melbourne, Victoria 3010, Australia. E-mail: c.boskovic@unimelb.edu.au*

[b]*Institute for Inorganic and Analytical Chemistry, Friedrich Schiller University Jena, Humboldtstraße 8, 07743 Jena, Germany*

[c]*CSIRO Manufacturing, Clayton, Victoria 3168, Australia*

[d]*Institute of Physical and Organic Chemistry, Southern Federal University, Rostov-on-Don, 344090, Russian Federation*

† Electronic supplementary information (ESI) available: Additional synthetic experimental details, TGA, powder X-ray diffraction, crystallographic data, structural analysis, IR, solid- and solution-state magnetic measurements, photomagnetism, UV-vis-NIR, mixed-valency analysis, electrochemistry, and DFT (PDF). DFT optimized *XYZ* coordinates of complexes (ZIP). CCDC 2393551–2393561. For ESI and crystallographic data in CIF or other electronic format see DOI: https://doi.org/10.1039/d4sc07798a

received increased attention.[15] In certain ligand environments, SCO is observed for Co(II) and Mn(III).[16] Valence tautomerism is most common for cobalt complexes with dioxolene (diox) redox-active ligands,[9,10] in which a LS-Co(III) centre coordinated to a catecholate ligand (LS-Co^{III}-cat) undergoes an intramolecular electron transfer and concerted spin transition to afford HS-Co(II)-semiquinonate (HS-Co^{II}-SQ). In contrast, VT involving a redox-active ligand in a discrete complex is significantly more unusual for iron (Table 1)[17–22] and manganese species.[23–25]

Unlike Co-dioxolene complexes, there are no discrete iron complexes that undergo VT with a spin transition occurring at the same time as electron transfer; either there is no spin-state change,[17–19] or electron transfer and spin transition occur sequentially.[20–22] Compounds [Fe(tpa)(3,6-dbdiox)]BF_4 and [(Fe(RR-cth))(Co(SS-cth))(DHBQ)]$(PF_6)_3$ (Chart S1†) (tpa = tris(2-pyridylmethyl)amine, 3,6-dbdiox = 3,6-di-*tert*-butyldioxolene, cth = 5,5,7,12,12,14-hexamethyl-1,4,8,11-tetra-azacyclotetradecane, $DHBQH_2$ = 2,5-dihydroxy-1,4-benzoquinone) were found to display a LS-Fe^{III}-cat ⇌ HS-Fe^{III}-cat SCO interconversion at low temperature, followed by a separate VT interconversion to HS-Fe^{II}-SQ at higher temperatures.[20,21] Alternative isolation of $[Fe(tpa)(3,6\text{-}dbdiox)]^+$ as the PF_6^-, BPh_4^- and ClO_4^- and $[(Fe(RR\text{-}cth))(Co(SS\text{-}cth))(DHBQ)]^{3+}$ as the AsF_6^- salts results in only Fe(III) SCO.[20,26] The complex $[Fe(4\text{-}MeO\text{-}bpi)_2]$ (4-MeO-bpiH = 4,4′-di-methoxy-bis(pyridyl-imino)isoindoline) undergoes a VT transition in the solid-state from LS-Fe^{II}-bpi^- to LS-Fe^{III}-$bpi^{2\cdot-}$, triggering SCO to HS-Fe^{III}-$bpi^{2\cdot-}$.[22] However, in solution $[Fe(4\text{-}MeO\text{-}bpi)_2]$ only adopts a HS-Fe^{II}-bpi^- state. As the observation of VT in these reported iron compounds is highly dependent on the solid-state environment, the VT process is unlikely to be molecular in origin.

In certain cases, in addition to the common use of temperature, light can induce SCO and VT.[12,27,28] For SCO, light stimulation is known as light-induced excited spin-state trapping (LIESST),[12,27] in which light irradiation generates a metastable HS state. Trapping of the HS form is promoted by a large change in the metal–ligand bond distances between the LS and HS state. For Fe(II), the change is significant (~0.2 Å), resulting in efficient LIESST.[12,27] For Fe(III), the smaller change (~0.13 Å) commonly results in rapid relaxation of the HS-Fe(III) metastable state, making Fe(III) LIESST rarer.[12] The analogous process for VT complexes, light-induced valence tautomerism (LIVT), is observed for many Co-dioxolene complexes.[13,28–30] However, to the best of our knowledge, no other metal complex has been shown to display LIVT, limiting the available chemical building blocks to engineer light-induced VT materials. Of the discrete iron complexes that display thermally-induced VT, none have been reported to undergo LIVT.[17–22,31] We hypothesize that is due to the lack of a concerted spin transition in the VT process, minimizing the differences in the iron–ligand bond lengths between the tautomers, resulting in rapid relaxation of the metastable state.

In this study, we aimed to discover new examples of SCO or VT complexes. The family of N-donor redox-active bis((aryl) imino)acenaphthene (Ar-BIAN) ligands are well suited for this goal. The Ar-BIAN ligand has comparable redox chemistry to dioxolene ligands, with accessible neutral Ar-BIAN^0 (L^0), mono-anionic radical Ar-BIAN$^{\cdot-}$ ($L^{\cdot-}$), and dianionic Ar-BIAN^{2-} (L^{2-}) states.[32,33] Unlike dioxolene ligands in their neutral quinone form, Ar-BIAN^0 will readily coordinate with a metal centre,[33] allowing for two possible redox-couples to achieve VT: $L^{2-}/L^{\cdot-}$ and $L^{\cdot-}/L^0$. In addition, the electronic properties of Ar-BIAN can be easily tuned *via* variation of the aryl groups.[34]

We have recently reported the use of Ar-BIAN ligands to generate a new example of cobalt VT; the complex $[Co(4\text{-}MeO\text{-}BIAN)_3]^0$ undergoes a LS-Co^{III}-$(L^{\cdot-})_3$ ⇌ HS-Co^{II}-$(L^0)(L^{\cdot-})_2$ interconversion in solution (4-MeO-BIAN = bis[(4-methoxy-phenyl)imino]acenaphthene) (Chart S2†).[35] In that same study, the compound $[Co^{II}(Ph\text{-}BIAN)_3](PF_6)_2$ (Ph-BIAN = bis((phenyl) imino)acenaphthene) remains as HS-Co^{II}-$(L^0)_3$, with no SCO to LS-Co^{II}-$(L^0)_3$ or VT to LS-Co^{III}-$(L^{\cdot-})(L^0)_2$.[35] For this work, we hypothesized that replacement of cobalt with manganese or iron could result in SCO and/or VT in several possible ways. The lower Mn(II) and Fe(II) oxidation potential compared to Co(II) could stabilize a M^{III}-$(L^{\cdot-})(L^0)_2$ ground state (M = Fe, Mn), such that a M^{III}-$(L^{\cdot-})(L^0)_2$ ⇌ M^{II}-$(L^0)_3$ VT interconversion occurs. Alternatively, resultant Fe^{II}-$(L^0)_3$, Fe^{III}-$(L^{\cdot-})(L^0)_2$, and Mn^{III}-$(L^{\cdot-})(L^0)_2$ states could show SCO.[16,36] Previously, the syntheses of $[Fe(Ph\text{-}BIAN)_3][FeCl_4]_2$ and $[Fe(Ph\text{-}BIAN)_3](BF_4)_2$ were

Table 1 Reported discrete octahedral iron complexes that display thermally-induced VT[a]

Compounds	Interconversion	Phase	Ref.
[Fe(bispicen)(Cl_4-diox)(Cl_4-SQ)]	HS-Fe^{III}-(cat)(SQ) ⇌ HS-Fe^{II}-$(SQ)_2$	Solution	17
[Fe(porphyrin)(thiolate)][b]	HS-Fe^{III}-$thiolate^-$ ⇌ HS-Fe^{II}-$thiyl^{\cdot}$	Solution	18
$[Fe(paap)_2]BF_4$	LS-Fe^{III}-$(ISQ)_2$ ⇌ LS-Fe^{II}-(IBQ)(ISQ)	Solid & solution	19
$[Co^{III}(\eta^5\text{-}C_{10}H_{15})_2][Fe(paap)_2]$	LS-Fe^{III}-$(AP)_2$ ⇌ LS-Fe^{II}-(ISQ)(AP)	Solid & solution	19
[Fe(tpa)(3,6-dbdiox)]BF_4	LS-Fe^{III}-cat ⇌ HS-Fe^{III}-cat ⇌ HS-Fe^{III}-SQ	Solid	20
$[(Fe(RR\text{-}cth))(Co(SS\text{-}cth))(DHBQ)](PF_6)_3$	LS-Fe^{III}-cat ⇌ HS-Fe^{III}-cat ⇌ HS-Fe^{III}-SQ	Solid	21
$[Fe(4\text{-}MeO\text{-}bpi)_2]$	LS-Fe^{II}-$(bpi^-)_2$ ⇌ LS-Fe^{III}-$(bpi^{\cdot2-})(bpi^-)$ ⇌ HS-Fe^{III}-$(bpi^{\cdot2-})(bpi^-)$	Solid	22

[a] Chart S1 displays representations of these complexes. [b] Four different porphyrin/thiolate ligands were utilized.[18] Bispicen = *N*,*N*′-bis(2-pyridylmethyl)-1,2-ethanediamine, Cl_4-$SQ^{\cdot-}$ = 3,4,5,6-tetrachlorosemiquinonate, Cl_4-diox = 3,4,5,6-tetrachlorodioxolene, $paapH_2$ = 2-(2-phenylazo)-anilino-4,6-di-*tert*-butylphenol, tpa = tris(2-pyridylmethyl)amine, 3,6-dbdiox = 3,6-di-*tert*-butyldioxolene, cth = 5,5,7,12,12,14-hexamethyl-1,4,8,11-tetra-azacyclotetradecane, $DHBQH_2$ = 2,5-dihydroxy-1,4-benzoquinone, 4-MeO-bpiH = 4,4′-di-methoxy-bis(pyridyl-imino) isoindoline. cat^{2-} = catecholate, $SQ^{\cdot-}$ = semiquinonate, AP^{2-} = amidophenolate, $ISQ^{\cdot-}$ = iminobenzosemiquinonate, IBQ = iminobenzoquinonate.

reported, although the electronic structure and magnetic properties were not investigated.[37]

We report the synthesis and analysis of a family of [M(Ph-BIAN)$_3$](BPh$_4$)$_2$ compounds, where M = Zn (**1**), Co (**2**), Mn (**3**) and Fe (**4**) (Fig. 1), with a view towards possible SCO or VT. Compound **1** was used as a reference for the M^{II}-$(L^0)_3$ state, and to study the spectroscopic and electrochemical properties of coordinated Ph-BIAN isolated from a redox-active metal. The detailed multi-technique experimental studies of this family of complexes have allowed us to deduce the electronic structure of **1**, **2**, **3** and **4**. Compound **4** undergoes the first example of thermally-induced iron valence tautomerism that occurs with a concerted spin-state change. In addition, **4** displays a photo-induced interconversion that is hypothesised to be LIVT.

Results and discussion

Synthesis

The homoleptic complexes [M(Ph-BIAN)$_3$]$^{2+}$ (M = Zn, Co, Mn, and Fe, Fig. 1) were synthesized (ESI) by combining three equivalents of Ph-BIAN with the corresponding M(II) salt in methanol (in air for **1**, **2** and **3**, under N_2 for **4**). The combination of the metal salts and Ph-BIAN yielded a yellow solution of **1**, orange solutions for **2** and **3**, and a dark green solution for **4**. Addition of two equivalents of BPh_4^- resulted in **1**, **2** and **3**, forming as orange solids, and **4** as a green solid. Crystals suitable for X-ray diffraction were grown by layering a saturated dichloromethane (DCM) solution with diethylether (Et_2O) for **1**, DCM solution with diisopropylether ($^iPr_2O$) for **2**, 1,2-dichloroethane (DCE) with $^iPr_2O$ for **3**, and an acetonitrile (MeCN) solution with $^iPr_2O$ for **4**. Bulk samples for **1**, **2** and **3** were recrystallized using DCE/$^iPr_2O$, and **4** using MeCN/$^iPr_2O$. Elemental analysis (EA) indicates solvation of compounds as **1**·1.5DCE·1.5$^iPr_2O$, **2**·DCE·1.6$^iPr_2O$, **3**·0.4$^iPr_2O$ and **4**·1.7$^iPr_2O$. Thermogravimetric analysis (Fig. S1†) supports the formulation of **1**, **2**, **3** and **4** as solvates; deviation between the solvation determined from EA and thermogravimetric analysis for **3** is attributed to partial desolvation during sample preparation for EA, and **4** exhibits concurrent desolvation and thermal-decomposition. The experimental powder X-ray diffraction (PXRD) patterns match with the associated simulated pattern, indicating phase purity for all four compounds (Fig. S2†). The dramatic colour difference of **4** as a solid and in solution compared to the similar colours of **1**, **2** and **3** provided an initial indication that complex **4** adopts a significantly different electronic structure compared to **1**, **2** and **3**.

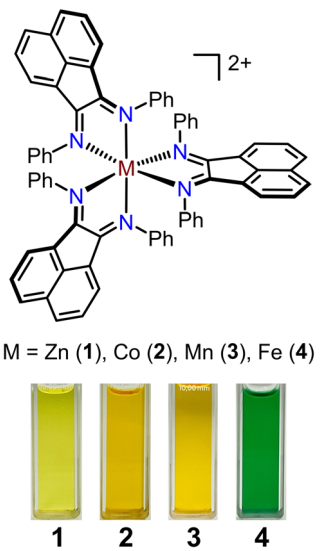

Fig. 1 Representation of the [M(Ph-BIAN)$_3$]$^{2+}$ metal complexes (M = Zn (**1**), Co (**2**), Mn (**3**), Fe (**4**), with numbering scheme. All complexes isolated as the BPh_4^- salt. Photographs of MeCN solutions of **1**, **2**, **3** and **4** at room temperature.

Solid-state analysis

Structure description. The structures of **1**, **2**, **3** and **4** were determined *via* single crystal X-ray diffraction (SCXRD) at 100 K (Tables S1 and S2†), providing key information regarding the electronic structure adopted in the solid-state. The colour of the crystals at 100 K is dark red for **1**, **2**, **3** and dark green for **4** (Fig. S3†). Compounds **1**·3DCM, **2**·DCM·2$^iPr_2O$ and **4**·2$^iPr_2O$ crystallize in the monoclinic *C*2/*c* space group with half a complex and one BPh_4^- anion in the asymmetric unit, and **3**·1.5$^iPr_2O$ crystallizes in the triclinic $P\bar{1}$ space group with a whole complex and two BPh_4^- anions in the asymmetric unit. The presence of two BPh_4^- anions per complex indicates an overall dicationic complex for **1**, **2**, **3** and **4**.

In the solid-state structures, all four complexes share a M(Ph-BIAN)$_3$ motif with a distorted octahedral geometry and approximate D_3 point symmetry (Fig. 2 and S4†). The oxidation and spin state of the metal centres can be determined by the M–N bond lengths, bond valence sum (BVS) parameters,[38] and octahedral distortion parameters (SHAPE index, Σ, and Θ).[39–41] The oxidation state of the Ph-BIAN ligands can be assigned *via* the α-diimine C–N and C–C bonds distances.[32,35,42] Neutral Ph-BIAN^0 has shorter C=N (1.28–1.31 Å) and longer C–C (1.46–1.53 Å) distances compared to the monoanionic Ph-BIAN$^{\bullet-}$ C=N (1.32–1.35 Å) and C–C (1.41–1.44 Å) bond lengths.[32,43]

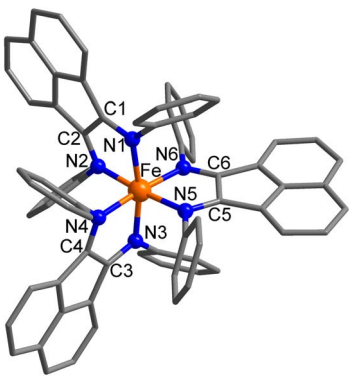

Fig. 2 Cationic structure of **4**·2$^iPr_2O$ at 100 K with relevant atoms labelled. Hydrogen atoms, solvent molecules, and BPh_4^- anions have been omitted for clarity. Colour code: C (dark grey), N (blue), Fe (orange).

Compound **1**·3DCM can only adopt a Zn^{II}-$(L^0)_3$ charge distribution. The average C=N and C–C bond distances of the three Ph-BIAN^0 ligands of 1.279(5) and 1.522(2) Å (Table 2 and Fig. S5†), respectively, deviate only slightly from the bond lengths of uncoordinated Ph-BIAN^0 (C=N: 1.275(2) Å, C–C 1.526(2) Å).[43] In both **2**·DCM·2^{i}Pr$_2$O and **3**·1.5^{i}Pr$_2$O, the long Co/Mn–N distances, large octahedral distortion, lack of Jahn–Teller distortion, and BVS values (Table 2 and Fig. S5†) are all consistent with HS-Co(II) and HS-Mn(II), respectively.[35,45] The C=N and C–C bond lengths for **2**·DCM·2^{i}Pr$_2$O and **3**·1.5^{i}Pr$_2$O are similar to those in **1** (Table 2 and Fig. S5†), indicating three Ph-BIAN^0 ligands. The lack of deviation in the C=N/C–C bond distances in **2** and **3** compared with **1** discount significant π-backbonding. Therefore, **1**, **2**, and **3** all adopt the same M^{II}-$(L^0)_3$ (**2** and **3** are HS) electronic form in the solid-state at 100 K.

In contrast, **4**·2^{i}Pr$_2$O (Fig. 2) exhibits significantly shorter Fe–N bond lengths and reduced octahedral distortion compared with **1**, **2** and **3** (Table 2). The Fe–N bond distances for LS-Fe(II) (1.95–2.05 Å) and LS-Fe(III) (1.95–2.09 Å) are shorter compared with HS-Fe(II) (2.15–2.21 Å) and HS-Fe(III) (2.09–2.15 Å).[36,46,47] Therefore, **4** is likely characterized by a LS-Fe(II) or LS-Fe(III) centre at 100 K, with the BVS value of 3.67 supporting the latter. The average Ph-BIAN C=N and C–C bonds are elongated and contracted, respectively, compared with **1**, **2** and **3** (Table 2 and Fig. S5†), and match with the distances observed for $[Co^{II}(\text{Ph-BIAN}^{\bullet-})(\text{Ph-BIAN}^0)_2]^+$ (C=N: 1.295(3) Å, C–C: 1.485(3) Å, Fig. S6†).[35] The bond lengths indicate one Ph-BIAN$^{\bullet-}$ and two Ph-BIAN^0 ligands, which are either crystallographically disordered or electronically delocalized. An overall dicationic charge is therefore consistent with **4**·2^{i}Pr$_2$O adopting the LS-Fe^{III}-$(L^{\bullet-})(L^0)_2$ electromer at 100 K in the solid-state. Overall, structural analysis shows that at 100 K, **1**, **2** and **3** adopt the M^{II}-$(L^0)_3$ electromeric state (**2** and **3** are HS), whereas **4** exists in the alternate LS-M^{III}-$(L^{\bullet-})(L^0)_2$ form. The different charge distribution of **4** explains the drastic colour variance of **4** compared to **1**, **2** and **3**.

Table 2 Selected interatomic distances (Å), distortion parameters, and BVS values for **1**·3DCM (M = Zn), **2**·DCM·2^{i}Pr$_2$O (M = Co), **3**·1.5^{i}Pr$_2$O (M = Mn), and **4**·2^{i}Pr$_2$O (M = Fe) at 100 K

	1·3DCM	**2**·DCM·2^{i}Pr$_2$O	**3**·1.5^{i}Pr$_2$O	**4**·2^{i}Pr$_2$O
M–N bond lengths/Å				
M–N_1	2.1734(9)	2.131(1)	2.262(1)	1.991(2)
M–N_2	2.193(1)	2.149(1)	2.242(1)	2.008(2)
M–N_3	2.1519(9)	2.124(1)	2.263(1)	1.991(2)
M–N_4	2.1519(9)	2.124(1)	2.283(1)	2.008(2)
M–N_5	2.193(1)	2.149(1)	2.268(1)	1.991(2)
M–N_6	2.1734(9)	2.131(1)	2.275(1)	1.991(2)
M–N_{av}	2.173(2)	2.135(2)	2.266(2)	1.997(5)
C–N/C–C bond lengths and interatomic distances/Å				
C_1–N_1	1.280(2)	1.274(2)	1.287(2)	1.292(3)
C_2–N_2	1.281(2)	1.285(2)	1.286(2)	1.295(3)
C_3–N_3	1.276(2)	1.275(2)	1.286(2)	1.292(3)
C_4–N_4	1.276(2)	1.275(2)	1.285(2)	1.295(3)
C_5–N_5	1.281(2)	1.285(2)	1.284(2)	1.292(3)
C_6–N_6	1.280(2)	1.274(2)	1.285(2)	1.292(3)
C–N_{av}	1.279(5)	1.278(5)	1.286(5)	1.293(7)
C_1–C_2	1.524(1)	1.507(2)	1.516(2)	1.482(3)
C_3–C_4	1.519(2)	1.500(2)	1.520(2)	1.482(3)
C_5–C_6	1.524(1)	1.507(2)	1.522(2)	1.480(4)
C–C_{av}	1.522(2)	1.505(3)	1.519(3)	1.481(6)
r_{AB}[a]	3.895(2)	3.843(2)	4.075(2)	3.632(3)
Distortion parameters				
SHAPE (O_h)[b]	1.271	1.175	2.015	0.665
Σ/°[c]	76.7	74.7	97.2	54.4
Θ/°[c]	242.1	237.0	296.1	177.6
BVS[d]	1.77	1.96	1.95	3.67

[a] Average distance (Å) between the three N–C–C–N centroids. [b] SHAPE index for octahedral geometry in SHAPE 2.1.[39,40] A value of 0 represents a perfect octahedron. [c] $\sum$ = sum of the deviation of the 12 N/O–Co–N/O angles from 90°. Θ = sum of the deviation of 24 unique torsional angles between the N/O atoms on opposite triangular faces of the octahedron from 60°, providing the degree of trigonal distortion from an octahedron to trigonal prism. These were calculated using OctaDist[39–41] – a program for determining the structural distortion of the octahedral complexes. For a perfect octahedron, $\sum$ and Θ are zero. [d] Bond valence sum.[38,44]

Variable temperature X-ray diffraction. To determine if **4**·2^{i}Pr$_2$O undergoes thermally induced VT or SCO from the LS-Fe^{III}-$(L^{\bullet-})(L^0)_2$ ground state, we collected additional structures between 100 and 400 K (Tables S2 and S3†). Between 100 to 300 K, the average Fe–N bond distance only marginally increases by 0.007 Å (Fig. 3 and Table S4†), consistent with a LS-Fe^{III}-$(L^{\bullet-})(L^0)_2$ state up to 300 K. Above 300 K, the average Fe–N bond length rapidly increases to 2.070(3) Å at 400 K (Fig. 3 and Table S4†), alongside increasing octahedral distortion (Fig. S7†). The coordinate bond elongation is indicative of either a LS-Fe^{III}-$(L^{\bullet-})(L^0)_2$ ⇌ HS-Fe^{III}-$(L^{\bullet-})(L^0)_2$ SCO or LS-Fe^{III}-$(L^{\bullet-})(L^0)_2$ ⇌ HS-Fe^{II}-$(L^0)_3$ VT interconversion. Compared to typical Fe–N lengths for HS-Fe(II) (2.15–2.21 Å)[36,47] and HS-Fe(III) (2.09–2.15 Å),[46] a SCO transition is approximated as 45–75% complete and a VT

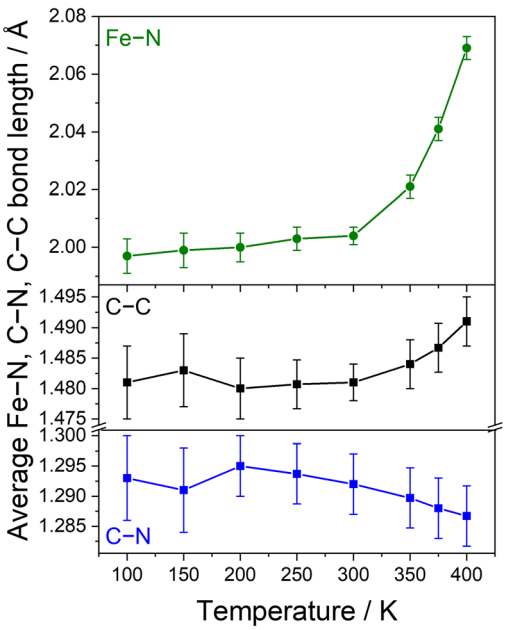

Fig. 3 Temperature dependence of the average Fe–N bond distances (top) and C–C and C–N bond distances of the Ph-BIAN ligands (bottom) for **4**·2^{i}Pr$_2$O.

transition is approximated as 35–45% complete at 400 K (Fig. S8†).

To aid differentiation between a SCO or VT transition, we analysed the changes to the C=N and C–C bond lengths of the Ph-BIAN ligands; VT would result in contraction and elongation, respectively, whereas no change is expected for SCO. The Ph-BIAN$^{\bullet-}$ ligand remains disordered across the three ligands at all temperatures (Table S4†). Between 300 and 400 K, the average C–C bond distances increase from 1.481(6) to 1.491(4) Å, and the average C=N lengths decrease from 1.293(7) to 1.287(5) Å (Fig. 3, S9 and Table S4†), in conjunction with the changes to the Fe–N bond lengths. Unfortunately, the errors of the averaged ligand bond lengths are too high to be able to determine if there is a ligand oxidation state change. The individual C–C and C=N bond distances increase and decrease with increasing temperature, respectively, some within the margin of error (Fig S9 and Table S4†). From the present structural data, we cannot definitively say if **4**·2^{i}Pr$_2$O undergoes SCO or VT; we tentatively suggest the VT transition LS-Fe^{III}-(L$^{\bullet-}$)(L^0)$_2$ ⇌ HS-Fe^{II}-(L^0)$_3$ in the solid-state.

Solid-state infrared and electronic spectroscopy. Infrared (IR) spectra of **1**·1.5DCE·1.5^{i}Pr$_2$O, **2**·DCE·1.6^{i}Pr$_2$O, **3**·0.4^{i}Pr$_2$O and **4**·1.7^{i}Pr$_2$O were acquired in the solid-state (Fig. 4 and S10†). The similarity of the spectra is consistent with **1**, **2**, **3** and **4** being isostructural. All four compounds share vibrational patterns associated with C=N stretches of neutral Ph-BAN^0 in the range 1700–1550 cm^{-1}.[35,42] The intensities (normalized to the most intense peak at 695 cm^{-1}) of these C=N stretches are comparable for **1**, **2** and **3** (Fig. 4), consistent with the coordination of three neutral Ph-BIAN^0 ligands and adoption of a M^{II}-(L^0)$_3$ state. In contrast, the intensity of these C=N stretches is markedly reduced in **4** (Fig. 4), which suggests less Ph-BIAN^0. A reduced amount of Ph-BIAN^0 is consistent with **4** adopting a LS-Fe^{III}-(L$^{\bullet-}$)(L^0)$_2$ electronic form in the solid-state at room temperature.

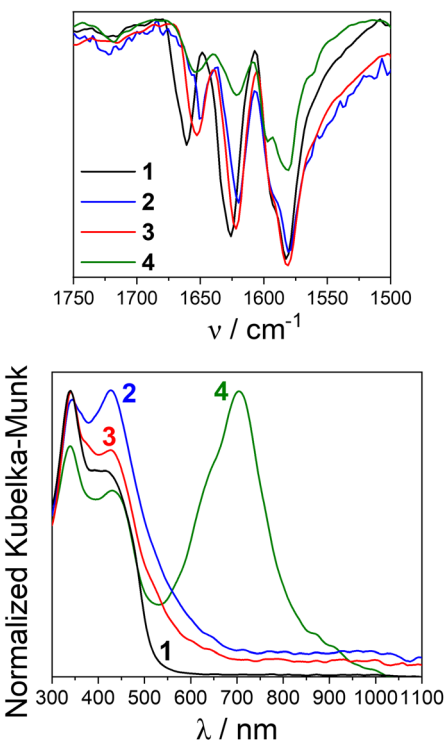

Fig. 4 Top: ATR-IR spectra of **1**·1.5DCE·1.5^{i}Pr$_2$O, **2**·DCE·1.6^{i}Pr$_2$O, **3**·0.4^{i}Pr$_2$O and **4**·1.7^{i}Pr$_2$O measured at room temperature in the C=N region between 1700–1500 cm^{-1}, normalized to the most intense peak at 695 cm^{-1}. Bottom: solid-state UV-vis spectra of **1**·1.5DCE·1.5^{i}Pr$_2$O, **2**·DCE·1.6^{i}Pr$_2$O, **3**·0.4^{i}Pr$_2$O and **4**·1.7^{i}Pr$_2$O measured as diffuse reflectance at room temperature, diluted ~5% in KBr.

Solid-state diffuse reflectance ultraviolet-visible (UV-vis) spectra were recorded for **1**·1.5DCE·1.5^{i}Pr$_2$O, **2**·DCE·1.6^{i}Pr$_2$O, **3**·0.4^{i}Pr$_2$O and **4**·1.7^{i}Pr$_2$O at room temperature (Fig. 4). The spectra for **1**, **2** and **3** are dominated by intraligand (IL) Ph-BIAN^0 processes centred at ~420 nm (resulting in the observed orange colour) and ~340 nm (Fig. 4).[35,42] No other features are observed that can be attributed to the presence of Ph-BIAN$^{\bullet-}$ or metal-to-ligand-charge transfer (MLCT) processes.[35,48,49] The presence of only Ph-BIAN^0 processes supports **1**, **2** and **3** adopting a M^{II}-(L^0)$_3$ tautomer in the solid-state at room temperature. Compound **4** also exhibits IL Ph-BIAN^0 processes in the solid-state (430, 340 nm, Fig. 4). In addition, **4** also features an intense peak at 700 nm, giving rise to the green colour. This process is not observed for free Ar-BIAN$^{\bullet-}$,[48] discounting a Ph-BIAN$^{\bullet-}$ ligand process. Instead, this feature is assigned as a Ph-BIAN$^{\bullet-}$ → Fe(III) ligand-to-metal charge transfer (LMCT), which would arise from the LS-Fe^{III}-(L$^{\bullet-}$)(L^0)$_2$ state adopted by **4** at room temperature.

Mössbauer spectroscopy. To determine if **4**·1.7^{i}Pr$_2$O undergoes the VT interconversion LS-Fe^{III}-(L$^{\bullet-}$)(L^0)$_2$ ⇌ HS-Fe^{II}-(L^0)$_3$, or the SCO interconversion LS-Fe^{III}-(L$^{\bullet-}$)(L^0)$_2$ ⇌ HS-Fe^{III}-(L$^{\bullet-}$)(L^0)$_2$ in the solid-state, we performed variable temperature, zero-field ^{57}Fe Mössbauer spectroscopy between 80 and 400 K (Fig. 5 and Table 3). At 80 K, a single quadrupole doublet with isomer shift $\delta = 0.393$ mm s^{-1} and a quadrupole splitting value of $\Delta E_Q = 0.456$ mm s^{-1} is observed, confirming a LS-Fe^{III}-(L$^{\bullet-}$)(L^0)$_2$ ground state.[50] The small quadrupole splitting compared to other reported LS-iron(III) complexes may be explained by the reduced octahedral distortion as apparent from single crystal X-ray diffraction. Heating up to 300 K does not result in significant changes to the spectrum, indicating the absence of SCO or VT up to room temperature, which is consistent with variable temperature SCXRD.

Upon increasing to 350 K, the doublet collapses to a broad singlet with $\delta = 0.348$ mm s^{-1} (Fig. 5 and Table 3), implying HS-Fe(III).[50] The broad shape is likely due to dynamic effects between LS-Fe(III) and HS-Fe(III) which occur faster than, or on, the timescale of the Mössbauer experiment (10^7–10^8 s^{-1}).[51] At 400 K, the spectrum is now characterized by a doublet at $\delta = 0.329$ mm s^{-1} (Fig. 5 and Table 3). The large quadrupole splitting of $\Delta E_Q = 0.919$ mm s^{-1} is not consistent with a symmetric HS-Fe(III) ($\Delta E_Q < 0.5$ mm s^{-1}) structure, and is therefore assigned as HS-Fe(II)[15] which would arise from formation of HS-Fe^{II}-(L^0)$_3$. Due to pronounced Doppler broadening of the resonance line at 400 K, identification of additional unresolved contributions (*e.g.* HS-Fe(III)) is impaired. However, given that

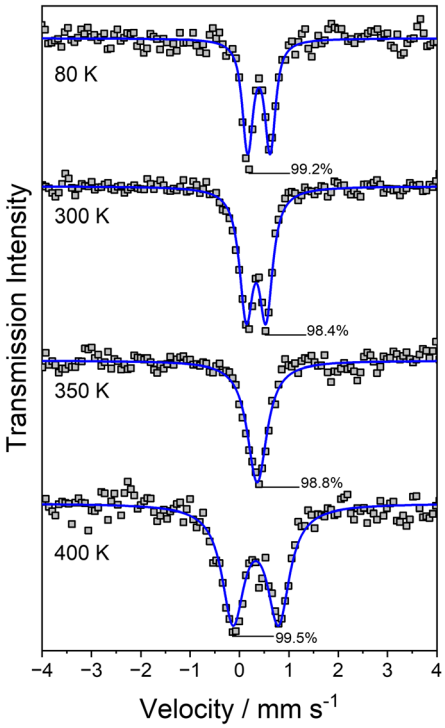

Fig. 5 Variable temperature, zero-field ^{57}Fe Mössbauer spectra of **4**·1.7^{i}Pr$_2$O. The squares are the raw data, and the solid lines are the least-square Lorentzian fits presented in Table 3.

Table 3 Selected ^{57}Fe Mössbauer parameters of **4**·1.7^{i}Pr$_2$O at different temperatures[a]

T/K	Oxidation & spin state	δ/mm s^{-1}	ΔE_Q/mm s^{-1}	Γ_{HWHM}/mm s^{-1}
80	LS-Fe(III)	0.393(10)	0.456(19)	0.111(14)
300	LS-Fe(III)	0.336(9)	0.399(15)	0.150(11)
350	LS/HS-Fe(III)	0.358(20)	—	0.231(29)
400	HS-Fe(II)	0.329(25)	0.919(46)	0.262(33)

[a] δ denotes the isomer shift, ΔE_Q is the quadrupole splitting, Γ_{HWHM} is the half width at half maximum. The ratio of relative intensities in doublets (A_2/A_1) is expected to be $A_2/A_1 = 1$. The value has therefore been fixed in the fit. Deviations from an ideal ratio may be attributed to *e.g.* texture effects due to preferred orientation of larger crystals relative to the γ-ray.[50]

the transition to HS-Fe(II) is not yet complete, this cannot be ruled out.

It appears that the transition first occurs with SCO from LS-Fe^{III}-(L$^{\bullet-}$)(L^0)$_2$ to HS-Fe^{III}-(L$^{\bullet-}$)(L^0)$_2$ (broad dynamic singlet at 350 K) followed by VT to HS-Fe^{II}-(L^0)$_3$ (doublet at 400 K), with both steps resolved by Mössbauer spectroscopy. From the present spectra, it cannot be determined if the VT interconversion in the solid-state has to proceed *via* HS-Fe^{III}-(L$^{\bullet-}$)(L^0)$_2$ before electron transfer, or if both LS-Fe^{III}-(L$^{\bullet-}$)(L^0)$_2$ and HS-Fe^{III}-(L$^{\bullet-}$)(L^0)$_2$ are able to undergo VT. It is possible that both LS-Fe^{III}-(L$^{\bullet-}$)(L^0)$_2$ ⇌ HS-Fe^{III}-(L$^{\bullet-}$)(L^0)$_2$ ⇌ HS-Fe^{II}-(L^0)$_3$ and LS-Fe^{III}-(L$^{\bullet-}$)(L^0)$_2$ ⇌ HS-Fe^{II}-(L^0)$_3$ are occurring, with the latter process possibly dominating at higher temperatures. Both SCXRD and solid-state magnetic measurements (see below) indicate that the process is not complete at 400 K. The observation of only one doublet at 400 K and the singlet at 350 K indicates fast dynamic effects and therefore averaged signals between the LS-Fe^{III}-(L$^{\bullet-}$)(L^0)$_2$ and the HS-Fe^{II}-(L^0)$_3$ species. Therefore, it is safe to assume that the quadrupole splitting of the pure HS-Fe^{II}-(L^0)$_3$ species will be even larger. In summary, Mössbauer spectroscopy confirms **4** has a LS-Fe^{III}-(L$^{\bullet-}$)(L^0)$_2$ ground state and undergoes an overall VT interconversion to HS-Fe^{II}-(L^0)$_3$.

Solid-state magnetic measurements. Variable temperature magnetic susceptibility measurements were performed for **2**·DCE·1.6^{i}Pr$_2$O, **3**·0.4^{i}Pr$_2$O and **4**·1.7^{i}Pr$_2$O. Compounds **2**·DCE·1.6^{i}Pr$_2$O and **3**·0.4^{i}Pr$_2$O were measured between 1.8 and 300 K. For **4**·1.7^{i}Pr$_2$O, data were collected upon cooling from 300 to 1.8 K, followed by heating to 400 K, cooling to 1.8 K, and heating to 400 K. Variable-field magnetization measurements are presented in Fig. S11.† Compound **2**·DCE·1.6^{i}Pr$_2$O exhibits a $\chi_M T$ of 2.9 cm^3 mol^{-1} K at 300 K (Fig. 6). The $\chi_M T$ is characteristic of a HS-Co(II) centre, in which spin–orbit coupling contributions result in a $\chi_M T$ higher than the spin-only value for $S = 3/2$ and $g = 2$ (1.88 cm^3 mol^{-1} K).[52] The $\chi_M T$ value remains essentially constant upon cooling to 100 K, before decreasing rapidly to 1.7 cm^3 mol^{-1} K at 1.8 K due to depopulation of the Co(II) spin–orbit coupled states. Therefore, magnetic data confirm that **2** adopts a temperature invariant HS-Co^{II}-(L^0)$_3$ state with no SCO or VT. Compound **3**·0.4^{i}Pr$_2$O displays an essentially temperature-independent $\chi_M T$ of 4.3–4.4 cm^3 mol^{-1} K between 1.8 and 300 K (Fig. 6), indicative of HS-Mn(II) ($S = 5/2$, theoretical $\chi_M T = 4.38$ cm^3 mol^{-1} K). Fitting the data with PHI afforded $g = 1.994(1)$ (Fig. S12†).[53] The low temperature magnetization data of **3**·0.4^{i}Pr$_2$O saturates at 5 μ_B (Fig. S11†), again consistent with an $S = 5/2$ ground state. Overall, magnetic data corroborate that **3** exists in a temperature invariant HS-Mn^{II}-(L^0)$_3$ state.

Compound **4**·1.7^{i}Pr$_2$O exhibits a $\chi_M T$ value of 0.1 cm^3 mol^{-1} K at 300 K, remaining essentially constant until 20 K, below which the $\chi_M T$ decreases to 0.05 cm^3 mol^{-1} K at 1.8 K (Fig. 6). A diamagnetic LS-Fe^{II}-(L^0)$_3$ state ($S = 0$) is discounted based on the structural and spectroscopic data. Instead, **4** is best interpreted as adopting a LS-Fe^{III}-(L$^{\bullet-}$)(L^0)$_2$ state between 1.8 and 300 K with strong antiferromagnetic coupling between Ph-BIAN$^{\bullet-}$ and LS-Fe(III). The magnetic data in the range 20–250 K were fit to the isotropic Heisenberg exchange Hamiltonian $\hat{H}_{ex} = -2J(\hat{S}_1 \cdot \hat{S}_2)$ (Fig. S13†) using PHI,[53] where J is the exchange interaction between LS-Fe(III) and Ph-BIAN$^{\bullet-}$ (both $S = 1/2$) and S_i are the corresponding spin operators, with g fixed to 2.0 for both spin centres. A good fit was achieved with $J = -700(40)$ cm^{-1} with the inclusion of temperature independent paramagnetic (TIP) = $9.4(2) \times 10^{-5}$ cm^3 mol^{-1} and a paramagnetic impurity (ρ) = 2.4(1)% that corresponds to residual paramagnetism from possible trapped HS-Fe(II) ($S = 2$). The rapid decrease below 20 K could be due to depopulation of the spin–orbit coupled states of trapped HS-Fe(II) and/or intermolecular antiferromagnetic exchange interactions. The Mössbauer spectroscopy data discount a VT transition from LS-Fe^{III}-(L$^{\bullet-}$)(L^0)$_2$ to LS-Fe^{II}-(L^0)$_3$ occurring up to 300 K, which that

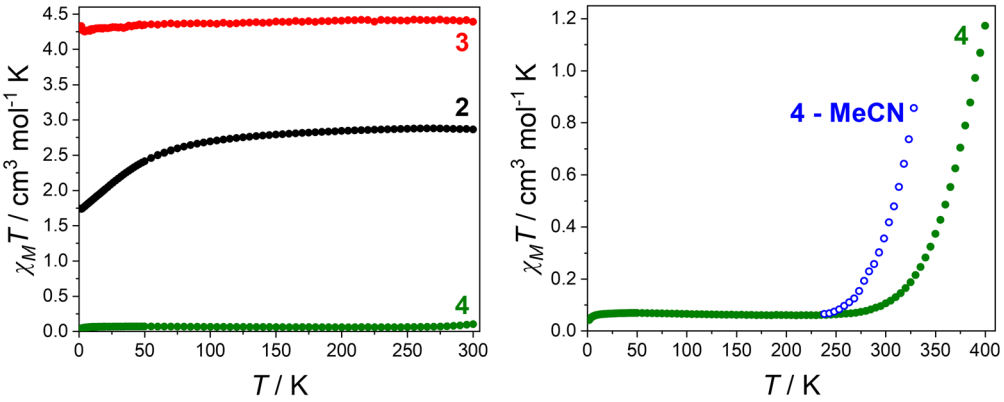

Fig. 6 Plots of $\chi_M T$ *vs.* T for **2**·DCE·1.6^{i}Pr$_2$O (black), **3**·0.4^{i}Pr$_2$O (red) and **4**·1.7^{i}Pr$_2$O (green) in the solid-state, and plots of $\chi_M T$ *vs.* T for **4** in d$_3$-MeCN (blue).

would not be detected by magnetometry due to a lack of spin state change.

Above 300 K, the $\chi_M T$ profile of **4**·1.7^{i}Pr$_2$O rapidly increases to 1.2 cm^3 mol^{-1} K at 400 K (Fig. 6). The feature is reversible (Fig. S14†). The reversible increase in $\chi_M T$ with temperature confirms the overall LS-Fe^{III}-(L$^{\bullet-}$)(L^0)$_2$ ⇌ HS-Fe^{II}-(L^0)$_3$ VT interconversion process tentatively suggested by SCXRD and shown by Mössbauer spectroscopy. The theoretical spin-only $\chi_M T$ value of HS-Fe^{II}-(L^0)$_3$ is 3.0 cm^3 mol^{-1} K, with experimental values for HS-Fe(II) ranging between 3.2–3.5 cm^3 mol^{-1} K due to spin–orbit contributions.[36,54] The VT transition is approximated as being ∼35–40% complete (Fig. S15†), matching the estimation from variable temperature SCXRD. Overall, magnetic data confirm that in the solid-state, compounds **2** and **3** do not display VT or SCO and adopt a temperature invariant HS-M^{II}-(L^0)$_3$ state. In contrast, magnetic measurements confirms that **4** adopts a LS-Fe^{III}-(L$^{\bullet-}$)(L^0)$_2$ ground state and undergoes an overall incomplete thermally-induced VT transition to HS-Fe^{II}-(L^0)$_3$ above 300 K.

Photomagnetic measurements. As mentioned in the Introduction, LIVT has not been reported for iron-based complexes that show thermally-induced VT,[17–22,31] which we suggest is due to the lack of a concerted spin transition accompanying electron transfer. Due to the spin-state change associated with the VT interconversion of **4** (mirroring Co-dioxolene VT), and therefore larger changes in the Fe–N bond lengths, we hypothesized LIVT could be possible in this case.

Photoirradiation of **4**·1.7^{i}Pr$_2$O at 10 K was performed using the setup represented in Fig. S16† by scanning the wavelengths between 280–500 nm (Fig. S17†) and 600–1000 nm, corresponding to the ligand-based and LMCT transitions, respectively. The largest response was observed for 420 nm, with photoirradiation for 12 hours resulting in an increase in $\chi_M T$ from 0.09 to 0.15 cm^3 mol^{-1} K (Fig. 7 and S18†). No photostationary limit was reached even after this 12 hour period. Repeating the measurement with a smaller amount of sample (0.3 mg *vs.* 0.8 mg) produced a larger photomagnetic response ($\chi_M T$ = 0.18 cm^3 mol^{-1} K) due to increased light penetration, but resulted in significantly noisier thermal data. The photomagnetic response is either the conversion of the LS-Fe^{III}-(L$^{\bullet-}$)(L^0)$_2$ ground state to a metastable HS-Fe^{II}-(L^0)$_3$ (LIVT, ∼5% conversion) or HS-Fe^{III}-(L$^{\bullet-}$)(L^0)$_2$ (LIESST, ∼3% conversion) state. Based on the thermal behaviour, we suggest **4** displays LIVT. On warming after 10 K irradiation, the curve rejoins the non-irradiated curve at ∼100 K (Fig. 7), resulting in a T(photoirradiation) value of 82 K. If this temperature corresponds to T(LIVT), it is in the upper range compared to values reported for Co-diox complexes (30–80 K).[29,55–58]

To investigate the relaxation features of the photoinduced state of **4**, isothermal relaxation profiles from the photoinduced state to the ground state were monitored by time-dependent magnetic susceptibility measurements at five temperatures upon irradiation at 420 nm (Fig. S19†). Unfortunately, the data are noisy due to the weakly paramagnetic nature of **4** and the limited photoconversion. The photoinduced fraction γ is defined as $\gamma(t) = (\mu_{DC}(t) - \mu_{DC\text{-off}})/(\mu_{DC\text{-}t=0} - \mu_{DC\text{-off}})$, where $\mu_{DC}(t)$ is the DC magnetic moment at time t, $\mu_{DC\text{-off}}$ is the DC magnetic moment without irradiation, and $\mu_{DC\text{-}t=0}$ is the DC magnetic moment reached at the end of the photoirradiation period (*i.e.*, at time t = 0 of the relaxation curve).[55,59] Over nine

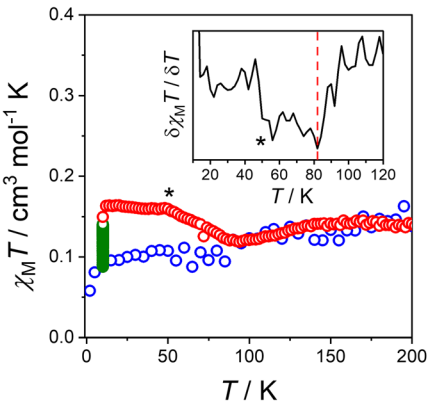

Fig. 7 Plot of $\chi_M T$ *vs.* T for **4**·1.7^{i}Pr$_2$O upon cooling (blue circles) response with irradiation with 420 nm for 12 hours at 10 K (green circles), and subsequent warming scan after the light is switched off (red circles). Inset figure shows $\delta\chi_M T/\delta T$ *vs.* T, with T(photoirradiation) indicated by the red line (82 K). * Bump due to molecular oxygen.

hours, γ decays by ~15% between 10–50 K, and ~25% at 60 K (Fig. S19†), representing a relatively large temperature range at which the photoinduced state remains trapped.

The shape of the decay curves for **4** match the stretched exponential decays observed for Co-diox LIVT complexes,[29,30,55–63] rather than the typical decay of LIESST compounds, which show self-acceleration processes best modelled by a sigmoidal function.[64,65] We propose that the stretched exponential decay, in conjunction with the thermal behaviour, indicates a photoinduced LS-Fe^{III}-($L^{\bullet-}$)(L^0)$_2$ ⇌ HS-Fe^{II}-(L^0)$_3$ VT interconversion. The decay curves were fit with a stretched exponential function $\gamma(t) = (1 - \gamma_{HS})e^{(-(t/\tau)^{\beta})} + \gamma_{HS}$ (Fig. S19†), where $\gamma(t)$ is the photoinduced fraction at time t, γ_{HS} is the equilibrium photoinduced fraction and **1** represents the photoinduced fraction at the end of the photoirradiation period ($t = 0$), τ is a decay constant (indicative of the time it takes the signal to have relaxed to $1/e$ of its initial value (at $t = 0$ s)), $0 < \beta \leq 1$ is a parameter accounting for the inhomogeneous distribution of spin-centres in the sample,[60–62,66] and the γ_{HS} value has been fixed to zero as it represents the HS photoinduced fraction as $t \rightarrow \infty$. The relaxation times (τ values) range 10^5–10^7 seconds (Table S5†). As the measurement time is 3.5×10^4 seconds, the extracted relaxation times have no physical meaning as they represent extrapolation of the measured relaxation times by 1–3 orders of magnitude.[57] Despite this, the relaxation of the metastable state of **4** is clearly slow over a large temperature range (10–80 K). The relaxation data, coupled with the high T(photoirradiation) value, suggest a highly stable photoinduced state with respect to temperature.

The combined solid-state analysis shows that **4** displays the thermally-induced VT interconversion LS-Fe^{III}-($L^{\bullet-}$)(L^0)$_2$ ⇌ HS-Fe^{II}-(L^0)$_3$, which might also be accessible with light (Scheme 1). If the VT interconversion can be light-induced, this would be the first for an Fe-based VT system. Future work is required to confirm the photoinduced metastable state is HS-Fe^{II}-(L^0)$_3$.

Computational study. Density functional theory (DFT) calculations were performed for the cationic complexes of **2**, **3** and **4** in the gas phase to study the relative energies of the different electronic states to support the solid-state observations. The electromer energies (E, kcal mol^{-1}) were calculated with UTPSSh/6-311++G(d,p),[67,68] which has been successful in modelling VT and SCO.[35,69–74] Compound **4** was also calculated with UOPBE/6-311++G(d,p),[46,72,75–77] as UTPSSh/6-311++G(d,p) over stabilizes LS-Fe(III/II) states.[70,78] Calculations indicate that **2** has a HS-Co^{II}-(L^0)$_3$ ground state (on the quartet potential energy surface (PES)) as observed experimentally (Table S6 and Fig. S20†). The calculated geometry matches the structure of **2**·DCM·2^iPr_2O at 100 K (Table S7†). The LS-Co^{II}-(L^0)$_3$ electromer (doublet PES) is destabilized by 3.8 kcal mol^{-1} (Table S6 and Fig. S20†). The LS-Co^{III}-($L^{\bullet-}$)(L^0)$_2$ state was not found as it is located on the same doublet PES as LS-Co^{II}-(L^0)$_3$, which is more symmetric and energetically preferred. Therefore, calculations discount SCO or VT. Compound **3** is calculated to have a HS-Mn^{II}-(L^0)$_3$ ground state (Table S6 and Fig. S21†), mirroring experimental results, with the calculated bond lengths matching well with those experimentally determined for **3**·1.5^iPr_2O (Table S7†). On the doublet PES, a LS-Mn^{II}-(L^0)$_3$ state was localized (ΔE = 5.4 kcal mol^{-1}), while the search for the electromer on the quartet PES resulted in the "broken symmetry" state (antiferromagnetic exchange between HS-Mn^{III} and $L^{\bullet-}$) of the HS-Mn^{III}-($L^{\bullet-}$)(L^0)$_2$ species (Table S6 and Fig. S21†). The latter structure is destabilized by 15.1 kcal mol^{-1}, and the attempts to find its high-spin state on the sextet PES (*i.e.* HS-Mn^{III}-($L^{\bullet-}$)(L^0)$_2$) invariably led to the most stable electromer HS-Mn^{II}-(L^0)$_3$. Unfortunately for **4**, both UTPSSh/6-311++G(d,p) and UOPBE/6-311++G(d,p) calculated an incorrect ground state (LS-Fe^{II}-(L^0)$_3$ and HS-Fe^{II}-(L^0)$_3$, respectively) (Tables S6, S8, Fig. S22 and S23†).

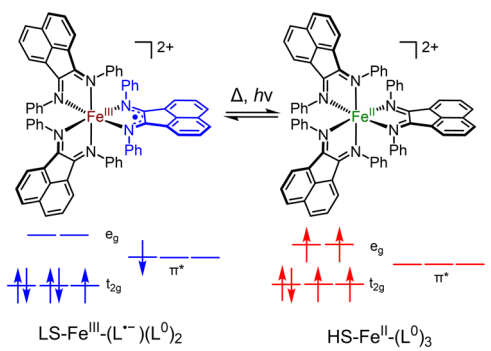

Scheme 1 Valence tautomeric equilibrium LS-Fe^{III}-($L^{\bullet-}$)(L^0)$_2$ ⇌ HS-Fe^{II}-(L^0)$_3$ displayed by **4** in the solid- and solution-state.

Solution-state analysis

The analysis in the solid state indicates that **1**, **2** and **3** do not display SCO or VT, adopting a M^{II}-(L^0)$_3$ electronic state (**2** and **3** are HS). In contrast, **4** displays an overall LS-Fe^{III}-($L^{\bullet-}$)(L^0)$_2$ ⇌ HS-Fe^{II}-(L^0)$_3$ VT interconversion. As demonstrated by previous Fe-VT compounds, the VT behaviour can be highly dependent on the surrounding chemical environment.[20–22] We therefore performed complementary solution studies to determine the electronic states exhibited by **1**, **2**, **3** and **4** in solution, with a focus on determining if the VT interconversion exhibited by **4** is molecular in origin or dependent on the extended chemical environment.

Solution-state electronic spectroscopy. Ultraviolet-visible-near-infrared (UV-vis-NIR) spectra were recorded for **1**, **2**, **3** and **4** at room temperature in various solvents with a range of dielectric constants (κ): MeCN (κ = 37.5), butyronitrile (BuCN) (κ = 20.7), dichloroethane (DCE) (κ = 10.4) and tetrahydrofuran (THF) (κ = 7.5) (Fig. 8 and S24†). Absorption bands and tabulated assignments are in Table S9.† The spectra of **1**, **2**, **3** and **4** remain unchanged over several hours, consistent with solution stability (**4** under N_2). Like the solid-state spectra, the solution spectra of **1**, **2** and **3** feature dominant IL Ph-BIAN^0 processes at ~400 nm and ~320 nm,[35,42] with no features associated with Ph-BIAN$^{\bullet-}$ (Fig. 8 and S25†). Therefore, **1**, **2** and **3** also adopt the M^{II}-(L^0)$_3$ state in solution at room temperature. The spectra of **4** across all four solvents are also similar to the solid-state spectrum, indicative of a predominant LS-Fe^{III}-($L^{\bullet-}$)(L^0)$_2$ state (Fig. 8 and S25†); the solution spectra feature IL Ph-BIAN^0 peaks at

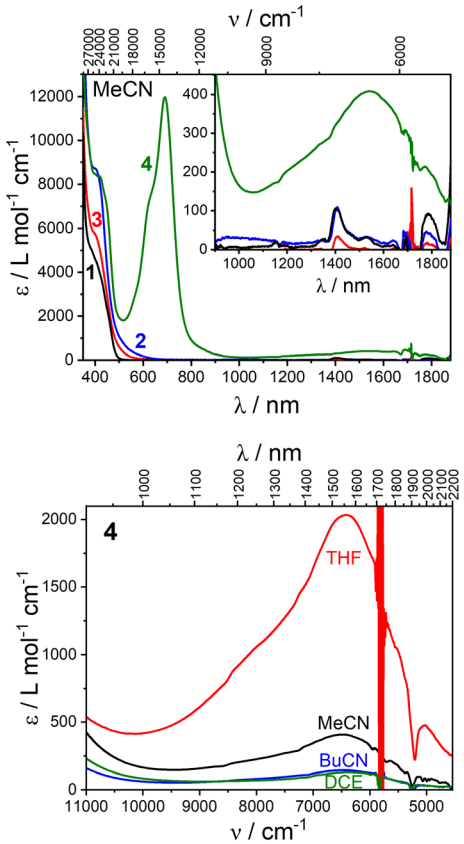

Fig. 8 Top: UV-vis-NIR spectra of **1**, **2**, **3** and **4** in MeCN at 298 K. Bottom: NIR spectra of **4** in MeCN, BuCN, DCE and THF at 298 K.

~420 and ~320 nm and a Ph-BIAN$^{\bullet-}$ → Fe(III) LMCT transition at ~690 nm. Overlapping the IL Ph-BIAN^0 process at 420 nm are lower energy peaks at ~430 and ~450 nm assigned as IL Ph-BIAN$^{\bullet-}$ processes (Fig. 8 and S26†).[35,48,49] Solvent identity can play a significant role in influencing a VT equilibrium.[35,79,80] The increased prominence of the LMCT and IL Ph-BIAN$^{\bullet-}$ processes in DCE *vs.* MeCN, BuCN and THF suggests increased population of LS-Fe^{III}-(L$^{\bullet-}$)(L^0)$_2$ in DCE.

The LS-Fe^{III}-(L$^{\bullet-}$)(L^0)$_2$ tautomeric state of **4** contains Ph-BIAN in two different oxidation states (neutral and monoanionic), which is an example of organic-based mixed-valence (MV).[81–83] Organic MV systems share similarities with the more common instance of mixed-valency in which the metal ions in a multinuclear complex differ in oxidation state. If compound **4** has a LS-Fe^{III}-(L$^{\bullet-}$)(L^0)$_2$ ground state and electronic coupling between the Ph-BIAN ligands, a ligand-to-ligand Ph-BIAN$^{\bullet-}$ → Ph-BIAN^0 intervalence charge transfer (IVCT) band should be observed in the near-infrared (NIR) region.[81–83] In the NIR region, **4** displays an IVCT band across all four solvents (~1550 nm, ~6450 cm^{-1}), confirming a LS-Fe^{III}-(L$^{\bullet-}$)(L^0)$_2$ state in solution at room temperature. Compounds **1**, **2** and **3** do not feature this IVCT band (Fig. 8), consistent with the non-MV M^{II}-(L^0)$_3$ state.

The degree of electronic coupling between the Ph-BIAN ligands in **4** can be described by the Robin and Day MV classification (class I, II, II–III. III, see ESI†)[84–87] and the electronic coupling parameter (H_{AB}), extracted from the energy and shape of the Ph-BIAN$^{\bullet-}$ → Ph-BIAN^0 IVCT band in the framework of Marcus-Hush theory.[88] These parameters have been used to define other metal complexes with MV ligands.[81,83] The presence of an IVCT band indicates intramolecular ligand-to-ligand electron transfer, discounting class I for **4**. The IVCT bands of **4** in MeCN, BuCN, DCE and THF were deconvoluted with two Gaussian functions (Fig. S27,† peak 1 at low energy, peak 2 at high energy), to extract ν_{max}, half-height-width ($\Delta\nu_{1/2}$) and molar absorptivity (ε_{max}) values (Table S10†). The MV class can be determined based on solvent-dependency: class II is solvent-dependent with $\Delta\nu_{max}$ > 200 cm^{-1} for a range of dielectric constant ($\Delta\kappa$) of 30, class II–III and III are solvent-independent with ($\Delta\nu_{max}$ < 200 cm^{-1}).[84–86] Across all four solvents used, ($\Delta\kappa$ = 30), peak 1 has a $\Delta\nu_{max}$ of ~120 cm^{-1} that suggests class II–III or III, and peak 2 has a $\Delta\nu_{max}$ of 300 cm^{-1}, suggesting class II (Table S10†). The cumulative fit has a $\Delta\nu_{max}$ of 100 cm^{-1} across all four solvents, giving a tentative assignment of class II–III. To support a possible MV II–III assignment, we used the Γ parameter (eqn (S6), see ESI† for details), determined from the peak width: for class II, Γ < 0.5, class II and II, $\Gamma \approx 0.5$, and class III, Γ > 0.5.[89] Across all four solvents, peaks 1 and 2 have Γ values of 0.64–0.66 and 0.06–0.38 (Table S10†) that support assignment of class II–III and II, respectively. Marcus-Hush analysis estimates H_{AB} values of 160–670 cm^{-1} for peak 1 and 230–920 cm^{-1} for peak 2 (Table S10 and eqn (S7)†) of **4**. The $2H_{AB}/\nu_{max}$ values of 0.05–0.22 for both bands suggest MV class II.[84–86] The strength of electronic coupling is comparable to other organic MV systems in transition metal complexes; H_{AB} values of 810–840 cm^{-1} for class II[90,91] and 920–1100 cm^{-1} for class II–III.[91,92] Overall, **4** is on the border of class II and II–III. Therefore, **4** has a localized electronic structure and solvent averaging, with a residual barrier to electron transfer arising from intramolecular structural changes.[85,86] The average of the Ph-BIAN^0 and Ph-BIAN$^{\bullet-}$ C=N/C–C bond lengths observed in the structure of **4**·2^{i}Pr$_2$O must be due to crystallographic disorder, not electronic delocalization.

The same analysis of the previously reported[35] IVCT band of [Co^{II}(Ph-BIAN$^{\bullet-}$)(Ph-BIAN^0)$_2$]$^+$ in MeCN and DCM indicate class II–III (Fig. S28 and Table S11†), with H_{AB} values of 1190–1380 cm^{-1} for peak 1 and 1190–1630 cm^{-1} for peak 2. The electronic coupling between the Ph-BIAN units in the LS-Fe^{III}-(L$^{\bullet-}$)(L^0)$_2$ state for **4** is weaker than for [Co^{II}(Ph-BIAN$^{\bullet-}$)(Ph-BIAN^0)$_2$]$^+$. We initially expected the shorter metal–ligand bond lengths in **4** that decrease the distance between the Ph-BIAN ligands to promote increased electron transfer. Analysis using electrochemistry (see Electrochemistry section) shows electron transfer actually occurs through the metal, with Co(II) facilitating more efficient electron transfer in [Co^{II}(Ph-BIAN$^{\bullet-}$)(Ph-BIAN^0)$_2$]$^+$ compared with Fe(III) in **4**. Previously, Fe(III) has been shown to be less effective than other 3d metals at promoting intramolecular electron transfer between ligands.[93] The class II/II–III IVCT behaviour for **4** indicates stronger coupling between the ligand centres compared to Fe(III) complexes with MV dioxolene ligands.[93,94] The difference between **4** and these Fe-dioxolene complexes is that **4** shows VT,[93,94] which would

increase electron density on the iron centre, resulting in more efficient electron transfer between the ligands.

Variable temperature electronic spectroscopy. To study whether **4** undergoes a LS-Fe^{III}-(L$^{\bullet-}$)(L^0)$_2$ ⇌ HS-Fe^{II}-(L^0)$_3$ VT interconversion in solution, we performed variable temperature UV-vis measurements in MeCN, BuCN, DCE and THF. The minimal changes in the spectra of **1**, **2** and **3** in BuCN between 268 and 373 K (Fig. S29 and S30†) is consistent with the absence of SCO and VT in solution. Distinct and reversible changes are evident for **4** in all solvents upon changing temperature (Fig. 9 and S31†). The 298 K spectra were recovered after the full measurement (Fig. S32†), indicating a reversible interconversion and thermal stability. Upon increasing the temperature of the solutions of **4**, the LMCT peak at ∼690 nm and the IL Ph-BIAN$^{\bullet-}$ peak at ∼420 nm reduce in intensity, and the three closely spaced peaks centred at ∼320 nm become a single peak (Fig. 9 and S31†). These changes are most obvious in BuCN with the widest temperature window (268–373 K, Fig. 9). The decrease in intensity of the LMCT and IL Ph-BIAN$^{\bullet-}$ bands suggests reduction in LS-Fe^{III}-(L$^{\bullet-}$)(L^0)$_2$ population upon heating, consistent with a LS-Fe^{III}-(L$^{\bullet-}$)(L^0)$_2$ ⇌ HS-Fe^{II}-(L^0)$_3$ VT interconversion.

The spectral profile of **4** upon heating (most evident in BuCN) approaches that of **1**, **2** and **3** (in BuCN at 373 K for comparison) (Fig. 9, S33 and S34†); specifically the loss of the LMCT band, replacement of the IL Ph-BIAN$^{\bullet-}$ peaks at ∼420 nm with IL Ph-BIAN^0 features, and the change in the peak shape at 320 nm. Therefore, the high temperature spectra of **4** resembles that expected for a HS-M^{II}-(L^0)$_3$ state, supporting the interpretation that **4** undergoes LS-Fe^{III}-(L$^{\bullet-}$)(L^0)$_2$ ⇌ HS-Fe^{II}-(L^0)$_3$ VT in solution. The difference in the spectra of the HS-M^{II}-(L^0)$_3$ state in **4** compared with **1**, **2** and **3** appears to be a peak at ∼620 nm, which we assign as a Fe(II) → Ph-BIAN^0 metal-to-ligand charge transfer (MLCT). Deconvolution of the spectra of **4** in BuCN between 268–373 K using the spectra of **1** in BuCN at the same temperature, and plotting the relative spectral area (430–1100 nm) yields a transition temperature ($T_{1/2}$) of ∼320 K (Fig. S35†). The observation of the same spectral change upon heating for **4** across all four solvents further supports that the observation of VT is not dependent on the surrounding chemical environment. The relative changes in the spectra of **4** upon heating (268–323 K, maximum collection temperature in THF), are greater in MeCN/BuCN compared with DCE/THF (Fig. S36†). The smaller change in the spectra with temperature in DCE and THF suggest these solvents stabilize the LS-Fe^{III}-(L$^{\bullet-}$)(L^0)$_2$ tautomer to a greater degree.

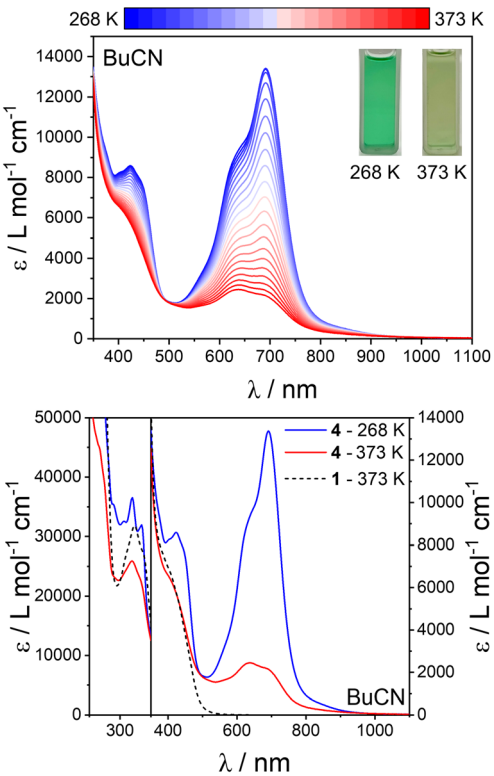

Fig. 9 Top: variable temperature UV-vis absorption spectra of **4** in BuCN between 268 (blue) and 373 K (red) in 5 K increments. Bottom: comparison of the UV-vis spectra of **4** in BuCN at 268 (blue) and 373 K (red) with **1** in BuCN at 373 K.

Solution-state magnetic measurements. To provide further evidence for the electronic states determined for **2**, **3** and **4** in solution, we performed solution magnetic measurements in d_3-MeCN using the Evans NMR method.[95] The room temperature solution $\chi_M T$ of **2** (3.0 cm^3 mol^{-1} K) and **3** (4.4 cm^3 mol^{-1} K) confirms a HS-Co^{II}-(L^0)$_3$ and HS-Mn^{II}-(L^0)$_3$ state, respectively. To corroborate the LS-Fe^{III}-(L$^{\bullet-}$)(L^0)$_2$ ⇌ HS-Fe^{II}-(L^0)$_3$ VT interconversion suggested by variable temperature UV-vis for **4**, we performed variable temperature solution magnetic susceptibility measurements between 238–328 K (as limited by the freezing and boiling point of d_3-MeCN). The $\chi_M T$ value of 0.1 cm^3 mol^{-1} K at 238 K for **4** is essentially diamagnetic, which is consistent with a LS-Fe^{III}-(L$^{\bullet-}$)(L^0)$_2$ state in solution at this temperature. The $\chi_M T$ product increases rapidly from 0.1 cm^3 mol^{-1} K at 238 K to 0.9 cm^3 mol^{-1} K at 328 K (Fig. 6), confirming a spin transition. Combined with the variable temperature UV-vis analysis, compound **4** undergoes the same VT interconversion in solution as observed in the solid-state.

The transition remains incomplete up to 328 K, but the transition temperature ($T_{1/2}$) in solution is shifted ∼50 K lower compared to the solid-state. To obtain thermodynamic quantities, we fit the solution susceptibility data with the regular solution model (eqn (S3)†). A fit was obtained with $(\chi_M T)_{max}$ = 3.5(9) cm^3 mol^{-1} K, ΔH = 30(2) kJ mol^{-1}, ΔS = 80(10) J K^{-1} mol^{-1}, and $T_{1/2}$ of 370(30) K (Fig. S37†). The values of ΔH and ΔS for **4** are similar to those reported for the VT interconversion of Co-dioxolene complexes in solution (ΔH = 31–37 kJ mol^{-1}, ΔS = 90–134 J K^{-1} mol^{-1}).[96–99] In Co-dioxolene VT complexes, the transition occurs either between spin = 1/2 and spin = 5/2 (ref. 97 and 99) (assume spin of 5/2 due to very weak magnetic exchange),[100] or spin = 0 and spin = 2 (ref. 96 and 98) (assume spin of 2 due to weak magnetic exchange),[52] resulting in Δspin = 2. For **4**, the transition also occurs with Δspin = 2 (from spin = 0 due to strong antiferromagnetic exchange between LS-Fe(III) and Ph-BIAN$^{\bullet-}$, and spin = 2 from HS-Fe(II)), resulting in similar thermodynamic parameters to Co-dioxolene VT. Overall, the charge distribution of **1**, **2**, **3** and **4** in the solution-state are

the same as in the solid-state. Crucially, variable temperature solution UV-vis and magnetic measurements confirm that the LS-Fe^{III}-$(L^{\bullet-})(L^0)_2$ ⇌ HS-Fe^{II}-$(L^0)_3$ VT transition displayed by **4** is molecular in origin.

Electrochemistry. The redox properties of **1**, **2**, **3** and **4** were investigated by cyclic voltammetry (CV) and rotating disk electrode (RDE) voltammetry in MeCN (Fig. 10, S38† and Table 4). The mid-point potentials (E_m) are reported for reversible processes, and the peak potentials (E_p) are reported for irreversible processes (Table 4). For reversible processes, the peak separation (ΔE_p) is given. From RDE, the half-wave potentials ($E_{1/2}$) and limiting currents (i_L) are reported. The position of zero current in the RDE (Fig. S38†) confirms assignments as either reduction or oxidation. For compound **1**, six reduction processes (I–VI) are observed in the measured potential window (Fig. 10), and an irreversible BPh_4^- oxidation (Fig. S38†).[101] As **1** adopts a Zn^{II}-$(L^0)_3$ state in solution, processes I, II and III are assigned as the sequential one-electron reductions of the three Ph-BIAN^0 ligands; $[Zn^{II}(\text{Ph-BIAN}^0)_3]^{2+}$ reduced to $[Zn^{II}(\text{Ph-BIAN}^{\bullet-})(\text{Ph-BIAN}^0)_2]^+$ (I), $[Zn^{II}(\text{Ph-BIAN}^{\bullet-})_2(\text{Ph-BIAN}^0)_2]$ (II), and $[Zn^{II}(\text{Ph-BIAN}^{\bullet-})_3]^-$ (III) (Fig. 10). As the limiting current of processes IV, V and VI suggests more than one electron per process (Fig. 10 and S38†), we tentatively assign processes IV–VI as involving reduction of the three Ph-BIAN$^{\bullet-}$ ligands at the α-diimine (to give Ph-BIAN^{2-}) and at the naphthalene backbone (giving Ph-BIAN$^{3\bullet-}$).[32,48]

The voltammograms of **2** and **3** share features with **1** (Fig. S38†). In the reduction scan, **2** also exhibits six reductions (I–VI), whereas **3** features five reductions, with process III potentially combined with IV. As for **1**, processes I, II and III in **2** and **3** are assigned as the sequential one-electron reduction of each of the three Ph-BIAN^0 ligands (Fig. 10). The limiting current for processes IV, V and VI are different for **2** and **3** compared to **1**, suggesting reduction of Ph-BIAN$^{\bullet-}$ and the Co(II)/Mn(II) centre. Upon oxidation, both **2** and **3** feature the BPh_4^- oxidation, and an additional oxidation process not observed for **1**. In compound **2**, process (VII) is assigned as a Co(II)/Co(III) oxidation.[35] For **3**, the oxidation (VIII) occurs at similar potential as the Mn(III)/Mn(IV) process observed for mononuclear manganese complexes with N_6 coordination sphere formed with pyridyl ligands.[45,102,103] The Mn(II)/Mn(III) oxidation of **3** is potentially hidden by the BPh_4^- process; the i_L in the RDE for **3** (145 μA) is 25% larger than the four-electron BPh_4^- process of **1** (115 μA) and **2** (120 μA), suggesting a five-electron process.

The separation between the potentials of processes I and II (Δ_L) is significantly different between **1** (160 mV), **2** (650 mV), and **3** (280 mV) (Fig. 10). The value of Δ_L provides an indication of the strength of electronic communication between the three Ph-BIAN ligands in the M^{II}-$(L^{\bullet-})(L^0)_2$ redox state, with increasing communication in the order **1** < **3** < **2**. The comproportionation constants (K_c) for **1**, **2** and **3**, calculated using $\log_{10}(K_c) = 17.2 \times \Delta_L$ (Δ_L in V),[85] are 5.6×10^2, 1.5×10^{11}, and 6.5×10^4, respectively. As the MV class for Co^{II}-$(L^{\bullet-})(L^0)_2$ (see Solution-state electronic spectroscopy section) is II–III, the smaller Δ_L for **1** and **3** suggests an MV class approaching/being II. Spectroelectrochemistry or isolation of $[Zn^{II}(\text{Ph-BIAN}^{\bullet-})(\text{Ph-BIAN}^0)_2]^+$ and $[Mn^{II}(\text{Ph-BIAN}^{\bullet-})(\text{Ph-BIAN}^0)_2]^+$ would be required to confirm the MV class of the M^{II}-$(L^{\bullet-})(L^0)_2$ state of **1** and **3**. A through-space origin of the variation of electronic communication between the three complexes is discounted; Ph-BIAN N–C–C–N centroid distances (Table 2) are similar for all three complexes, and no significant structural changes upon reduction occurs.[35] Instead, ligand communication must occur *via* the coordination bonds. We hypothesize that as the degree of metal–ligand covalency increases, together with the degree of metal character in these predominantly ligand-centred reductions, electronic delocalization also increases.[91,104,105] The extent of covalency arises from the amount of overlap between the metal d-orbitals and the Ph-BIAN singly occupied molecular orbital (SOMO).[104,105] For Co(II), the d-orbitals and SOMO have similar energies, increasing covalency and enhancing electron transfer. For Mn(II), the reduction in d-orbital energy relative to the SOMO reduces covalency, weakening electronic coupling. The redox-inactive Zn(II) has negligible metal–ligand covalency, minimising interligand electron transfer. Increased covalency between the metal centre and Ph-BIAN results in stabilisation of the $[M^{II}(\text{Ph-BIAN}^{\bullet-})(\text{Ph-BIAN}^0)_2]^+$ redox state; this manifests as an increase in the potential of process I in the order **1** < **3** < **2**.

The voltammogram of **4** exhibits six reduction processes (I–VI), the BPh_4^- oxidation, and an additional oxidation process (VIII) (Fig. S38†). The assignment of the processes for **4** are complicated by the presence of concomitant VT in MeCN solution at room temperature, and the possibility for both ligand- and metal-based processes. Process I could be either reduction of the Fe(III) centre (Fe^{II}-$(L^{\bullet-})(L^0)_2$) or reduction of Ph-

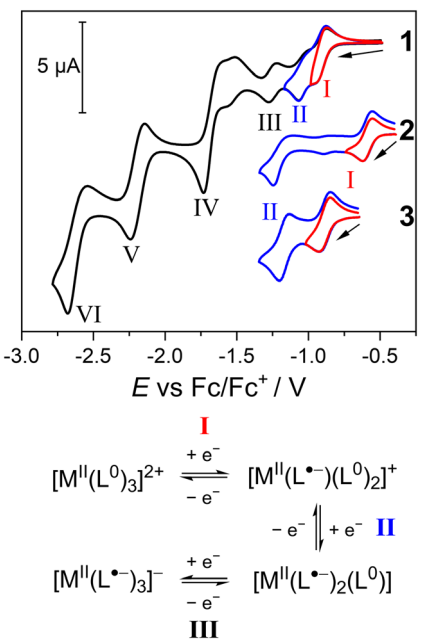

Fig. 10 Top: cyclic voltammograms of process I, II, III, IV, V and VI for compound **1**, and processes I and II for compounds **2** and **3** (1.0 mM MeCN solutions with 0.25 M Bu_4NPF_6) obtained with a scan rate of 100 mV s^{-1}. Arrow indicates direction of measurement, with all measurements started at position of zero current. Bottom: assignment of the redox processes I, II and III for complexes **1**, **2** and **3**.

Table 4 CV and RDE data for **1**, **2**, **3** and **4** in MeCN[a]

	Process								
	I	II	III	IV	V	VI	BPh_4^-	VII	VIII
Cyclic voltammetry $E_m$or E_{pa}/V (ΔE_p/mV)[b]									
1	−0.91(80)	−1.07[c]	−1.25(50)	−1.73[c]	−2.19(100)	−2.61(140)	0.47[c]	—	—
2	−0.59(65)	−1.24[c]	−1.43(68)	−1.71[c]	−2.17(85)	−2.67[c]	0.46[c]	0.68[c]	—
3	−0.89(75)	−1.17(65)	−1.78[c]		−2.27(115)	−2.75[c]	0.43[c]	—	1.04[c]
4	−0.67(70)	−1.18(68)	−1.7[c,d]	−1.74[c]	−2.32(110)	−2.71[c]	0.45[c]	—	1.01(65)
Rotating disk electrode voltammetry $E_{1/2}$/V(i_L/μA)[b]									
1	−0.91(24)	−1.09(18)	−1.26(17)	−1.76(65)	—	—	0.50(120)	—	—
2	−0.59(20)	−1.24(23)	−1.44(20)	−1.73(64)	—	—	0.45(115)	—	—
3	−0.87(22)	−1.17(30)	−1.79(108)[e]		—	—	0.43(145)	—	—
4	−0.67(23)	−1.19(25)	−1.66(30)	−1.75(32)	—	—	0.43(140)	—	1.03(20)

[a] Potentials reported *vs.* Ferrocene/Ferrocenium couple, measured as 65–75 mV with CV under the same conditions. Error in potentials is ±5 mV. [b] 1.0 mM in MeCN with 0.25 M Bu_4NPF_6, scan rate 100 mV s^{-1}. [c] E_p rather than E_m. [d] Only an estimation as the process is obscured by IV. [e] Processes combined due to close spacing.

$BIAN^0$ (Fe^{III}-($L^{\bullet-}$)$_2$(L^0)), with subsequent processes II and III potentially involving either/both metal and ligand orbitals. If process I is indeed the reduction of Fe(III), **4** has a Δ_L of 510 mV. The degree of ligand communication in the M^{II}-($L^{\bullet-}$)(L^0)$_2$ redox state would therefore increase in the order **1** < **3** < **4** < **2**. This trend is consistent with previous observations that Fe(II) and Co(II) enhance delocalisation compared to Zn(II) and Mn(II).[104,105] Spectroelectrochemistry or isolation of a reduced derivative of **4** is required to confirm whether process I is metal- or ligand-based. The oxidation process VIII could be assigned as Ph-$BIAN^{\bullet-}$ oxidation; however, the potential appears too high for this oxidation process.[106] The Ph-$BIAN^{\bullet-}$ oxidation is possibly obscured by the BPh_4^- oxidation, with the i_L of 140 (compared with 120 for **1** and 115 for **2**) suggesting a five-electron process.

Conclusions

The aim of this work at the outset was to find new examples of metal–ligand pairings that display molecular switchability in the form of VT and/or SCO. Building on past studies that identified VT in a Co-Ar-BIAN complex,[35] we report the synthesis of [Zn(Ph-BIAN)$_3$](BPh$_4$)$_2$ (**1**), [Co(Ph-BIAN)$_3$](BPh$_4$)$_2$ (**2**), [Mn(Ph-BIAN)$_3$](BPh$_4$)$_2$ (**3**), and [Fe(Ph-BIAN)$_3$](BPh$_4$)$_2$ (**4**). The green colour of **4** compared to the orange coloured **1**, **2** and **3** suggested immediately that **4** adopts a different charge distribution. Combined structural, IR and UV-vis-NIR spectroscopy, magnetic susceptibility and computational analysis shows **1**, **2** and **3** adopt a temperature-invariant M^{II}-(L^0)$_3$ state, with **2** and **3** being HS, in the solid- and solution-states. Electrochemical analysis demonstrated that the metal centre modulates the degree of communication between the three coordinated Ph-BIAN ligands; increased covalency between the metal and ligand enhances electronic communication.

In contrast to **1**, **2** and **3**, comprehensive investigation unambiguously confirms that **4** exhibits a LS-Fe^{III}-($L^{\bullet-}$)(L^0)$_2$ ground state in both the solid- and solution-states. Solid-state structural, magnetic, and Mössbauer spectroscopy measurements demonstrate that **4** undergoes a thermally-induced overall VT transition from LS-Fe^{III}-($L^{\bullet-}$)(L^0)$_2$ to HS-Fe^{II}-(L^0)$_3$. Solution-state variable temperature UV-vis and magnetic measurements confirm this VT process is molecular in origin, and not dependent on solid-state packing effects. Therefore, this is the first instance of a thermally-induced VT transition in an iron complex with a redox-active ligand that occurs with a spin-state transition accompanying electron transfer. Solid-state photomagnetic measurements indicate a possible light-induced LS-Fe^{III}-($L^{\bullet-}$)(L^0)$_2$ ⇌ HS-Fe^{II}-(L^0)$_3$ VT interconversion. The photoinduced metastable state of **4** is highly stable with respect to temperature. Light-induced VT (LIVT) has not previously been observed for complexes other than cobalt-dioxolene. We attribute the possible LIVT for this Fe complex to the unique concerted spin-state transition accompanying electron transfer, which results in large changes to the Fe–N bond lengths. Future work would focus on confirming the identity of the metastable state.

This study indicates that an iron complex can undergo a thermally-induced VT interconversion that proceeds with a concerted spin-state change. This spin-state change is likely crucial to any LIVT. The key to achieving a VT process with a spin transition is therefore to utilize a ligand that can support both VT and a spin-state transition. The Ph-BIAN ligand is redox-active with an orbital energy that matches iron (VT), and has a free ligand N···N distance (2.84 Å) that falls within a range for diimine ligands that gives Fe^{II}(diimine)$_3$ SCO (2.78–2.93 Å).[35] Future work targeting Fe-LIVT should use ligands that satisfy these criteria.

In summary, all data are consistent with **4** undergoing LS-Fe^{III}-($L^{\bullet-}$)(L^0)$_2$ ⇌ HS-Fe^{II}-(L^0)$_3$ valence tautomerism in both the solid- and solution-state, which can be induced thermally, and potentially with visible light (Scheme 1). This represents a new type of valence tautomerism, in which an iron complex displays both electron transfer and a concerted spin-state change. This work suggests that LIVT could be possible for systems other than Co-dioxolene, with LIVT potentially beneficial for

applications in devices such as single-molecule junctions. As the percentage of photoconversion is low, future work should focus on decreasing the temperature of the thermally-induced VT transition in related iron complexes. A principal finding is that the metal centre with a conserved ligand set can modulate the magnetic switching behaviour. The system investigated, $[M(Ph\text{-}BIAN)_3]^{2+}$, is extremely electronically versatile, offering multiple avenues for VT and SCO. Incorporation of other metal centres, substituents on the aryl ring, and/or isolation of different oxidation states are all possible paths toward new spin transitions.

Data availability

Crystallographic data for all compounds have been deposited with the CCDC under deposition numbers 2393551–2393561 and can be obtained from **https://www.ccdc.cam.ac.uk/**. Other data are available from the authors upon reasonable request.

Author contributions

Conceptualization: JTJ, CB; investigation and formal analysis: JTJ, DSB, FD, IHI, RWG, MAH, RJM, AAS; funding acquisition: CB; project administration: CB; resources: CB, RJM, BW; supervision: CB, MJG, BW; visualization: JTJ; writing – original draft: JTJ, CB; writing – review & editing: all authors. All authors have given approval to the final version of the manuscript.

Conflicts of interest

There are no conflicts to declare.

Acknowledgements

C. B. thanks the Australian Research Council for funding (FT190100293). We acknowledge the Australian Research Council for an equipment grant (LE210100009). J. T. J. acknowledges support from the Australian Government for a Research Training Stipend, and the Dr Albert Shimmins Fund for an Albert Shimmins Postgraduate Writing Up Award. M. J. G. thanks the University of Melbourne for a Melbourne Post-doctoral Fellowship. F. D. acknowledges financial support of the Deutsche Forschungsgemeinschaft (project no. 509879467). A. A. S. thanks the Ministry of Science and Higher Education of the Russian Federation (State assignment in the field of scientific activity, project no. FENW-2023-0017). We thank Stanley Bagio for assistance with the graphics. This work was performed in part at the Trace Analysis for Chemical, Earth and Environmental Sciences (TrACEES) Platform at the University of Melbourne. This research was undertaken in part using the MX1 and MX2 beamlines at the Australian Synchrotron, part of ANSTO, Australia and made use of the Australian Cancer Research Foundation (ACRF) detector (for MX2).

References

1 C. J. Yu, S. Von Kugelgen, D. W. Laorenza and D. E. Freedman, *ACS Cent. Sci.*, 2021, **7**, 712–723.
2 E. Resines-Urien, M. Á. G. García-Tuñón, M. García-Hernández, J. A. Rodríguez-Velamazán, A. Espinosa and J. S. Costa, *Adv. Sci.*, 2022, **9**, 1–7.
3 A. Cornia and P. Seneor, *Nat. Mater.*, 2017, **16**, 505–506.
4 J. Villalva, A. Develioglu, N. Montenegro-Pohlhammer, R. Sánchez-de-Armas, A. Gamonal, E. Rial, M. García-Hernández, L. Ruiz-Gonzalez, J. S. Costa, C. J. Calzado, E. M. Pérez and E. Burzurí, *Nat. Commun.*, 2021, **12**, 1–8.
5 S. K. Karuppannan, A. Martín-Rodríguez, E. Ruiz, P. Harding, D. J. Harding, X. Yu, A. Tadich, B. Cowie, D. Qi and C. A. Nijhuis, *Chem. Sci.*, 2021, **12**, 2381–2388.
6 H. J. Shepherd, I. A. Gural'Skiy, C. M. Quintero, S. Tricard, L. Salmon, G. Molnár and A. Bousseksou, *Nat. Commun.*, 2013, **4**, 1–9.
7 M. D. Manrique-Juárez, S. Rat, L. Salmon, G. Molnár, C. M. Quintero, L. Nicu, H. J. Shepherd and A. Bousseksou, *Coord. Chem. Rev.*, 2016, **308**, 395–408.
8 P. Gütlich and H. A. Goodwin, *Top. Curr. Chem.*, 2004, 1–47.
9 T. Tezgerevska, K. G. Alley and C. Boskovic, *Coord. Chem. Rev.*, 2014, **268**, 23–40.
10 G. K. Gransbury and C. Boskovic, in *Encyclopedia of Inorganic and Bioinorganic Chemistry*, Wiley, 2021, pp. 1–24.
11 D. Aguilà, Y. Prado, E. S. Koumousi, C. Mathonière and R. Clérac, *Chem. Soc. Rev.*, 2016, **45**, 203–224.
12 M. Nakaya, R. Ohtani, L. F. Lindoy and S. Hayami, *Inorg. Chem. Front.*, 2021, **8**, 484–498.
13 O. Sato, A. Cui, R. Matsuda, J. Tao and S. Hayami, *Acc. Chem. Res.*, 2007, **40**, 361–369.
14 A. Summers, F. Zahra, M. Zahir, G. F. Turner, M. A. Hay, A. Riboldi-Tunnicliffe, R. Williamson, S. Boer, L. Goerigk, C. Boskovic and S. A. Moggach, *Nat. Commun.*, 2024, **15**, 8922.
15 D. J. Harding, P. Harding and W. Phonsri, *Coord. Chem. Rev.*, 2016, **313**, 38–61.
16 J. Olguín, *Coord. Chem. Rev.*, 2020, **407**, 213148.
17 N. Shaikh, S. Goswami, A. Panja, X. Y. Wang, S. Gao, R. J. Butcher and P. Banerjee, *Inorg. Chem.*, 2004, **43**, 5908–5918.
18 P. K. Das, S. Samanta, A. B. McQuarters, N. Lehnert and A. Dey, *Proc. Natl. Acad. Sci. U. S. A.*, 2016, **113**, 6611–6616.
19 A. Rajput, A. K. Sharma, S. K. Barman, D. Koley, M. Steinert and R. Mukherjee, *Inorg. Chem.*, 2014, **53**, 36–48.
20 M. Chegerev, O. Demidov, P. Vasilyev, N. Efimov, S. Kubrin, A. Starikov, V. Vlasenko, A. Piskunov, S. Shapovalova, A. Guda, Y. Rusalev and A. Soldatov, *Dalton Trans.*, 2022, **51**, 10909–10919.
21 P. Sadhukhan, S.-Q. Wu, J. I. Long, T. Nakanishi, S. Kanegawa, K. Gao, K. Yamamoto, H. Okajima, A. Sakamoto, M. L. Baker, T. Kroll, D. Sokaras, A. Okazawa, N. Kojima, Y. Shiota, K. Yoshizawa and O. Sato, *Nat. Commun.*, 2021, **12**, 3–8.

22 A. Scheja, D. Baabe, D. Menzel, C. Pietzonka, P. Schweyen and M. Bröring, *Chem.–Eur. J.*, 2015, **21**, 14196–14204.
23 A. S. Attia and C. G. Pierpont, *Inorg. Chem.*, 1995, **34**, 1172–1179.
24 A. Caneschi and A. Dei, *Angew. Chem., Int. Ed.*, 1998, **37**, 3005–3007.
25 A. Panja, *Inorg. Chem. Commun.*, 2012, **24**, 140–143.
26 X. Zhang, W. H. Xu, W. Zheng, S. Q. Su, Y. B. Huang, Q. Shui, T. Ji, M. Uematsu, Q. Chen, M. Tokunaga, K. Gao, A. Okazawa, S. Kanegawa, S. Q. Wu and O. Sato, *J. Am. Chem. Soc.*, 2023, **145**, 15647–15651.
27 J. F. Létard, *J. Mater. Chem.*, 2006, **16**, 2550–2559.
28 D. M. Adams, B. Li, J. D. Simon and D. N. Hendrickson, *Angew. Chem., Int. Ed.*, 1995, **34**, 1481–1483.
29 K. G. Alley, G. Poneti, P. S. D. Robinson, A. Nafady, B. Moubaraki, J. B. Aitken, S. C. Drew, C. Ritchie, B. F. Abrahams, R. K. Hocking, K. S. Murray, A. M. Bond, H. H. Harris, L. Sorace and C. Boskovic, *J. Am. Chem. Soc.*, 2013, **135**, 8304–8323.
30 W. H. Xu, Y. B. Huang, W. W. Zheng, S. Q. Su, S. Kanegawa, S. Q. Wu and O. Sato, *Dalton Trans.*, 2024, **53**, 2512–2516.
31 J. Guasch, L. Grisanti, S. Jung, D. Morales, G. D'Avino, M. Souto, X. Fontrodona, A. Painelli, F. Renz, I. Ratera and J. Veciana, *Chem. Mat.*, 2013, **25**, 808–814.
32 I. L. Fedushkin, A. A. Skatova, V. A. Chudakova and G. K. Fukin, *Angew. Chem., Int. Ed.*, 2003, **42**, 3294–3298.
33 I. S. Fomenko, N. F. Romashev and A. L. Gushchin, *Coord. Chem. Rev.*, 2024, **514**, 215845.
34 M. Gasperini, F. Ragaini and S. Cenini, *Organometallics*, 2002, **21**, 2950–2957.
35 M. A. Hay, J. T. Janetzki, V. J. Kumar, R. W. Gable, R. Clérac, A. A. Starikova, P. J. Low and C. Boskovic, *Inorg. Chem.*, 2022, **61**, 17609–17622.
36 H. Phan, J. J. Hrudka, D. Igimbayeva, L. M. Lawson Daku and M. Shatruk, *J. Am. Chem. Soc.*, 2017, **139**, 6437–6447.
37 M. Villa, D. Miesel, A. Hildebrandt, F. Ragaini, D. Schaarschmidt and A. Jacobi von Wangelin, *ChemCatChem*, 2017, **9**, 3203–3209.
38 P. H. C. Camargo, *J. Mater. Sci.*, 2017, **52**, 9959–9962.
39 S. Llunell, M. Casanova, D. Cirera, J. Alemany and P. Alvarez, *SHAPE 2.1*, 2013.
40 S. Alvarez, D. Avnir, M. Llunell and M. Pinsky, *New J. Chem.*, 2002, **26**, 996–1009.
41 R. Ketkaew, Y. Tantirungrotechai, P. Harding, G. Chastanet, P. Guionneau, M. Marchivie and D. J. Harding, *Dalton Trans.*, 2021, **50**, 1086–1096.
42 V. L. Nadurata, M. A. Hay, J. T. Janetzki, G. K. Gransbury and C. Boskovic, *Dalton Trans.*, 2021, **50**, 16631–16646.
43 M. Schmitz, M. Seibel, H. Kelm, S. Demeshko, F. Meyer and H.-J. Krüger, *Angew. Chem., Int. Ed.*, 2014, **53**, 5988–5992.
44 I. D. Brown and D. Altermatt, *Acta Crystallogr., Sect. B: Struc. Sci., Crys. Eng., Mat.*, 1985, **244**, 244–247.
45 N. R. East, C. Förster, L. M. Carrella, E. Rentschler and K. Heinze, *Inorg. Chem.*, 2022, **61**, 14616–14625.
46 J. T. Janetzki, M. G. Chegerev, G. K. Gransbury, R. W. Gable, J. K. Clegg, R. J. Mulder, G. N. L. Jameson, A. A. Starikova and C. Boskovic, *Inorg. Chem.*, 2023, **62**, 15719–15735.
47 J. A. Real, M. C. Muñoz, J. Faus and X. Solans, *Inorg. Chem.*, 1997, **36**, 3008–3013.
48 I. L. Fedushkin, A. A. Skatova, V. A. Chudakova, V. K. Cherkasov, G. K. Fukin and M. A. Lopatin, *Eur. J. Inorg. Chem.*, 2004, 388–393.
49 I. L. Fedushkin, A. A. Skatova, M. Hummert and H. Schumann, *Eur. J. Inorg. Chem.*, 2005, 1601–1608.
50 P. Gütlich; E. Bill and A. X. Trautwein, *Mössbauer Spectroscopy and Transition Metal Chemistry: Fundamentals and Applications*, Springer, 2011.
51 Y. Maeda, N. Tsutsumi and Y. Takashima, *Inorg. Chem.*, 1984, **266**, 2440–2447.
52 G. K. Gransbury, M.-E. Boulon, R. A. Mole, R. W. Gable, B. Moubaraki, K. S. Murray, L. Sorace, A. Soncini and C. Boskovic, *Chem. Sci.*, 2019, **10**, 8855–8871.
53 N. F. Chilton, R. P. Anderson, L. D. Turner, A. Soncini and K. S. Murray, *J. Comput. Chem.*, 2013, **34**, 1164–1175.
54 L. J. Kershaw Cook, R. Kulmaczewski, R. Mohammed, S. Dudley, S. A. Barrett, M. A. Little, R. J. Deeth and M. A. Halcrow, *Angew. Chem., Int. Ed.*, 2016, **55**, 4327–4331.
55 F. Yu, M. Xiang, Q. G. Wu, H. He, S. Q. Cheng, X. Y. Cai, A. H. Li, Y. M. Zhang and B. Li, *Inorg. Chim. Acta*, 2015, **426**, 146–149.
56 P. Dapporto, A. Dei, G. Poneti and L. Sorace, *Chem.–Eur. J.*, 2008, **14**, 10915–10918.
57 R. D. Schmidt, D. A. Shultz and J. D. Martin, *Inorg. Chem.*, 2010, **49**, 3162–3168.
58 G. Poneti, M. Mannini, B. Cortigiani, L. Poggini, L. Sorace, E. Otero, P. Sainctavit, R. Sessoli and A. Dei, *Inorg. Chem.*, 2013, **52**, 11798–11805.
59 Y. Mulyana, G. Poneti, B. Moubaraki, K. S. Murray, B. F. Abrahams, L. Sorace and C. Boskovic, *Dalton Trans.*, 2010, **39**, 4757–4767.
60 A. Cui, K. Takahashi, A. Fujishima and O. Sato, *J. Photochem. Photobiol., A*, 2004, **167**, 69–73.
61 C. Carbonera, A. Dei, C. Sangregorio and J. F. Létard, *Chem. Phys. Lett.*, 2004, **396**, 198–201.
62 A. Beni, C. Carbonera, A. Dei, J. F. Létard, R. Righini, C. Sangregorio and L. Sorace, *J. Braz. Chem. Soc.*, 2006, **17**, 1522–1533.
63 A. Beni, A. Dei, S. Laschi, M. Rizzitano and L. Sorace, *Chem.–Eur. J.*, 2008, **14**, 1804–1813.
64 A. Hauser, C. Enachescu, M. L. Daku, A. Vargas and N. Amstutz, *Coord. Chem. Rev.*, 2006, **250**, 1642–1652.
65 A. Hauser, *Top. Curr. Chem.*, 2004, 55–198.
66 R. V. Chamberlin, G. Mozurkewich and R. Orbach, *Phys. Rev. Lett.*, 1984, **52**, 867–870.
67 J. Tao, J. P. Perdew, V. N. Staroverov and G. E. Scuseria, *Phys. Rev. Lett.*, 2003, **91**, 146401.
68 V. N. Staroverov, G. E. Scuseria, J. Tao and J. P. Perdew, *J. Chem. Phys.*, 2003, **119**, 12129–12137.
69 G. K. Gransbury, B. N. Livesay, J. T. Janetzki, M. A. Hay, R. W. Gable, M. P. Shores, A. Starikova and C. Boskovic, *J. Am. Chem. Soc.*, 2020, **142**, 10692–10704.
70 T. Tezgerevska, E. Rousset, R. W. Gable, G. N. L. Jameson, E. C. Sañudo, A. Starikova and C. Boskovic, *Dalton Trans.*, 2019, **48**, 11674–11689.

71 J. Cirera, M. Via-Nadal and E. Ruiz, *Inorg. Chem.*, 2018, **57**, 14097–14105.
72 O. S. Siig and K. P. Kepp, *J. Phys. Chem. A*, 2018, **122**, 4208–4217.
73 T. E. Fischer, J. T. Janetzki, F. Z. M. Zahir, R. W. Gable, A. A. Starikova and C. Boskovic, *Dalton Trans.*, 2024, **53**, 3104–3117.
74 J. T. Janetzki, G. K. Gransbury, R. W. Gable, M. J. Giansiracusa, A. A. Starikova and C. Boskovic, *Eur. J. Inorg. Chem.*, 2024, **27**, e202400227.
75 M. G. Chegerev and A. A. Starikova, *Comput. Theor. Chem.*, 2022, **1211**, 113693.
76 J. Sirirak, D. Sertphon, W. Phonsri, P. Harding and D. J. Harding, *Int. J. Quantum Chem.*, 2017, **117**, 1–8.
77 M. Swart, *J. Chem. Theory Comput.*, 2008, **4**, 2057–2066.
78 Y. Hitomi, M. Higuchi, H. Minami, T. Tanaka and T. Funabiki, *Chem. Commun.*, 2005, 1758–1760.
79 F. Z. M. Zahir, M. A. Hay, J. T. Janetzki, R. W. Gable, L. Goerigk and C. Boskovic, *Chem. Sci.*, 2024, **15**, 5694–5710.
80 V. L. Nadurata and C. Boskovic, *Inorg. Chem. Front.*, 2021, **8**, 1840–1864.
81 A. Arnold, T. J. Sherbow, R. I. Sayler, R. D. Britt, E. J. Thompson, M. T. Muñoz, J. C. Fettinger and L. A. Berben, *J. Am. Chem. Soc.*, 2019, **141**, 15792–15803.
82 J. Hankache and O. S. Wenger, *Chem. Rev.*, 2011, **111**, 5138–5178.
83 B. J. O. Kessler, I. F. Mansoor, D. I. Wozniak, T. J. Emge and M. C. Lipke, *J. Am. Chem. Soc.*, 2023, **145**, 15924–15935.
84 D. M. D'Alessandro, A. C. Topley, M. S. Davies and F. R. Keene, *Chem.–Eur. J.*, 2006, **12**, 4873–4884.
85 D. M. D'Alessandro and F. R. Keene, *Chem. Soc. Rev.*, 2006, **35**, 424–440.
86 K. D. Demadis, C. M. Hartshorn and T. J. Meyer, *Chem. Rev.*, 2001, **101**, 2655–2685.
87 P. Robin and M. B. Day, *Adv. Inorg. Chem. Radiochem.*, 1967, **10**, 247–422.
88 C. Creutz, in *Progress in Inorganic Chemistry*, 2007, pp. 1–73.
89 B. S. Brunschwig, C. Creutz and N. Sutin, *Chem. Soc. Rev.*, 2002, **31**, 168–184.
90 T. Kojima, F. Ogishima, T. Nishibu, H. Kotani, T. Ishizuka, T. Okajima, S. Nozawa, Y. Shiota, K. Yoshizawa, H. Ohtsu, M. Kawano, T. Shiga and H. Oshio, *Inorg. Chem.*, 2018, **57**, 9683–9695.
91 C. H. Yu, X. Yang, X. Ji, C. H. Wang, Q. Lai, N. Bhuvanesh and O. V. Ozerov, *Inorg. Chem.*, 2020, **59**, 10153–10162.
92 I. F. Mansoor, D. I. Wozniak, Y. Wu and M. C. Lipke, *Chem. Commun.*, 2020, **56**, 13864–13867.
93 C. G. Pierpont, *Inorg. Chem.*, 2011, **50**, 9766–9772.
94 A. S. Attia, S. Bhattacharya and C. G. Pierpont, *Inorg. Chem.*, 1995, **34**, 4427–4433.
95 D. F. Evans, *J. Chem. Soc.*, 1959, 2003–2005.
96 G. K. Gransbury, M. E. Boulon, S. Petrie, R. W. Gable, R. J. Mulder, L. Sorace, R. Stranger and C. Boskovic, *Inorg. Chem.*, 2019, **58**, 4230–4243.
97 D. M. Adams and D. N. Hendrickson, *J. Am. Chem. Soc.*, 1996, **118**, 11515–11528.
98 A. Dei, A. Feis, G. Poneti and L. Sorace, *Inorg. Chim. Acta*, 2008, **361**, 3842–3846.
99 D. M. Adams, A. Dei, A. L. Rheingold and D. N. Hendrickson, *J. Am. Chem. Soc.*, 1993, **115**, 8221–8229.
100 M. W. Lynch, R. M. Buchanan, C. G. Pierpont and D. N. Hendrickson, *Inorg. Chem.*, 1981, **20**, 1038–1046.
101 P. K. Pal, S. Chowdhury, M. G. B. Drew and D. Datta, *New J. Chem.*, 2002, **26**, 367–371.
102 S. Romain, C. Baffert, C. Duboc, J. C. Leprêtre, A. Deronzier and M. N. Collomb, *Inorg. Chem.*, 2009, **48**, 3125–3131.
103 S. Romain, C. Duboc, F. Neese, E. Rivière, L. R. Hanton, A. G. Blackman, C. Philouze, J. C. Leprêtre, A. Deronzier and M. N. Collomb, *Chem.–Eur. J.*, 2009, **15**, 980–988.
104 C. C. Lu, E. Bill, T. Weyhermüller, E. Bothe and K. Wieghardt, *J. Am. Chem. Soc.*, 2008, **130**, 3181–3197.
105 C. Fleming, S. Vu, D. J. R. Brook, S. Agrestini, E. Pellegrin and J. DaRos, *Front. Chem.*, 2023, **11**, 1–14.
106 R. A. Zarkesh, A. S. Ichimura, T. C. Monson, N. C. Tomson and M. R. Anstey, *Dalton Trans.*, 2016, **45**, 9962–9969.